

Early prodromal sensory neuropathy in Pink1-SNCA double mutant Parkinson mice

Lucie Valek

Goethe-Universität Frankfurt am Main Fachbereich 16 Medizin

Bao Tran

Goethe-Universität Frankfurt am Main Fachbereich 16 Medizin

Annett Wilken-Schmitz

Goethe-Universität Frankfurt am Main Fachbereich 16 Medizin

Sandra Trautmann

Goethe-Universität Frankfurt am Main Fachbereich 16 Medizin

Juliana Heidler

Goethe-Universität Frankfurt am Main Fachbereich 16 Medizin

Tobias Schmid

Goethe-Universität Frankfurt am Main Fachbereich 16 Medizin

Bernhard Brüne

Goethe-Universität Frankfurt am Main Fachbereich 16 Medizin

Dominique Thomas

Goethe-Universität Frankfurt am Main Fachbereich 16 Medizin

Thomas Deller

Goethe-Universität Frankfurt am Main Fachbereich 16 Medizin

Gerd Geisslinger

Goethe-Universität Frankfurt am Main Fachbereich 16 Medizin

Georg Auburger

Goethe-Universität Frankfurt am Main Fachbereich 16 Medizin

Irmgard Tegeder (✉ itegeder@hotmail.com)

Goethe University Frankfurt <https://orcid.org/0000-0001-7524-8025>

Research article

Keywords: Parkinson's Disease, pain, sensory loss, alpha-synuclein, PTEN inducible kinase 1, glucosylceramides, innate immunity, mitochondrial respiration

Posted Date: March 31st, 2020

DOI: <https://doi.org/10.21203/rs.3.rs-18284/v1>

License: © ⓘ This work is licensed under a Creative Commons Attribution 4.0 International License.

[Read Full License](#)

Abstract

BACKGROUND: Parkinson's Disease (PD) is frequently associated with a prodromal sensory neuropathy, which manifests as sensory loss and eventually chronic pain.

METHODS: The present study assessed somatosensory functions and the pathology of somatosensory neurons in Pink1^{-/-}-SNCAA53T double mutant mice (Pink1SNCA) who develop a PD-like disease > 15 months of age.

RESULTS: Pink1SNCA mice showed the first manifestations of sensory dysfunctions at 6 months of age, which were characterized by a loss of thermal sensitivity but sparing of mechanical sensation, and decline of olfactory perception of pleasant odors. Mechanistically, the loss of thermal sensitivity was attributed to a strong reduction of transient receptor potential TRPV and TRPA channels at mRNA, protein and functional levels in the dorsal root ganglia (DRGs). Primary sensory neurons responded much less to stimulations with capsaicin, formalin or depolarization as assessed by calcium imaging. RNA sequencing pointed to additional deregulations of voltage dependent potassium channel subtypes, lowering of acidic fibroblast growth factor driven support, and alterations of sphingolipid metabolism. Analyses of sphingolipids of multiple classes revealed an accumulation of glucosylceramides mainly in the DRGs and loss of sphingosines and sphinganine in the sciatic nerve. Transmission electron microscopy of the DRGs revealed a higher frequency of neurons with swollen mitochondria, which was associated with a decrease of mitochondrial respiration in sensory ganglia, but not in the brain.

CONCLUSION: The data support the view of a prodromal sensory disease in PD resulting from a combination of lipid allostasis and mitochondrial damage. Hence, Pink1SNCA mice phenocopy the PD-associated prodromal sensory neuropathy and reveal novel mechanistic insight.

Background

Parkinson's Disease (PD) is a complex neurodegenerative disease that primarily affects motor systems of the basal ganglia, and manifests with muscle rigidity, tremor, slowness of movement, and difficulty of walking [1]. PD also involves multiple extranigral regions and the peripheral nervous system [2] leading to non-motor symptoms, particularly olfactory dysfunctions, rapid eye movement (REM) sleep disorder, dysautonomia, restless leg disorder [3–7] and chronic pain that presents as neuropathic, visceral, musculoskeletal, dystonic pain and headaches and is highly prevalent in PD patients [8–12].

PD pain often precedes motor impairments [13] and is frequently associated with small or mixed fiber sensory neuropathies involving somatosensory and autonomic nerves [14–18]. Patients mostly complain about constipation, visceral discomfort and pain, gut and bladder dysfunctions and deregulation of exocrine glands, whereas a loss of somatosensation often remains unnoticed, unless it is associated with pain [19]. The progressive loss of sensory functions parallels the progression of the disease, but may precede motor symptoms for more than 10 years [13, 19] suggesting that sensory neurons are particularly vulnerable and likely represent a source of the propagation of prion-like alpha-synuclein [20–22].

The predominant morphological features of PD are intraneuronal alpha-synuclein-rich deposits, the major components of Lewy bodies [2, 23, 24], but the pathophysiology is only partly understood. Mitochondrial damage, dysfunctions of protein degradation via the proteasome and via autophagolysosomes contribute to the progressive loss of dopaminergic and other neurons. Defective mitophagy can lead to leakage of mitochondrial DNA to the cytosol that triggers innate immune system responses. In addition, it has been recognized in recent years that metabolic deregulations of bioactive lipids including ceramides and their metabolites increase the toxicity of alpha-synuclein [25–27]. Patients who are heterozygous carriers of glucocerebrosidase (GBA1) mutations tend to develop a rapidly progressive disease [28], and such mutations propagate alpha synuclein deposition in PD model organisms [29–32]. GBA1 is a lysosomal enzyme that catalyzes the degradation of ceramides to glucosylceramides (GlcCer) and subsequent generation of lactosylceramides (LacCer) and gangliosides. Low GBA1 activity and accumulations of GlcCer even occur in PD patients without known mutations of GBA1 [33, 34] and point to a link between PD and lysosomal storage disorders [35].

Indeed we have recently observed in patients with sporadic PD that high concentrations of plasma GlcCer are associated with pain ratings and with sensory losses as assessed via quantitative sensory testing, suggesting that GlcCer may contribute to the progression of the disease from peripheral sensory neurons to the brain and to clinical PD-associated pain (accompanying manuscript). There are no apparent remedies to specifically alleviate PD-associated pain or prevent sensory losses [36, 37] in part owing to limited knowledge of PD-associated somatosensory pathology in model organisms.

Motor functions and morphological characteristics of PD have been studied in several rodent-, primate- and fly models of the disease, but sensory functions and underlying pathological features of sensory neurons were rarely addressed [38] and the few studies of non-motor manifestations such as olfaction, anxiety-like behavior and gastrointestinal functions are fragmented and in part inconclusive.

In the present study, we used a previously described double mutant mouse model of PD to study pre-motor sensory phenomena and biological and morphological correlates in primary somatosensory neurons of these mice to understand better the underlying pathophysiological mechanisms and the progressive nature of the sensory loss. The mice carry a loss of function knock-in mutation of PTEN induced kinase (Pink1) and they are heterozygous for the human A53T mutation of alpha synuclein (SNCA-A53T). These Pink1SNCA mice develop spontaneous motor function deficits at advanced ages with an incidence of about 30% above 15 months of age. We show that sensory deficits occur much earlier and are associated with a prominent loss of transient receptor potential channels, mitochondrial damage and alterations of bioactive lipid patterns in somatosensory ganglia and peripheral nerves strengthening the pathological role of glucosylceramides.

Methods

Mouse strains

Homozygous $Pink1^{-/-}$ plus SNCA A53T double mutant mice were generated by crossing $Pink1^{-/-}$ mice (background: 129/SvEv) with A53T-SNCA-overexpressing PrPmtA mice (background: FVB/N) and then, interbreeding the littermates. They contain 129/SvEv and FVB/N genetic backgrounds approximately in a 50:50 distribution. Wildtype (WT) control mice are hybrids from a crossbreeding of 129/SvEv and FVB/N mice, which were descended from littermates of the respective single mutant animals. The double mutant mice are referred to as $Pink1^{-/-}$ -SNCA^{A53T} or in short, Pink1SNCA.

Mice had free access to food and water, and they were maintained in climate-controlled rooms with a 12 h light-dark cycle. Behavioral experiments were performed between 10 am and 3 pm. The experiments were approved by the local Ethics Committee for animal research (Darmstadt, Germany), adhered to the guidelines for pain research in conscious animals of the International Association for the Study of PAIN (IASP) and those of the Society of Laboratory Animals (GV-SOLAS) and were in line with the European and German regulations for animal research.

Analysis of nociception and somatosensory functions

Nociceptive tests were performed at 2, 4, 10 and 12 months of age with 8 mice per group. Mice were habituated to the test room and the test chambers for three consecutive days before the baseline measurement.

The latency of paw withdrawal on pointy mechanical stimulation was assessed using a Dynamic Plantar Aesthesiometer (Ugo Basile, Comerio, Italy). The steel rod was pushed against the plantar paw with ascending force (0–5 g, over 10 s, 0.2 g/s) and then maintained at 5 g until the paw was withdrawn. The paw withdrawal latency was the mean of three consecutive trials with at least 30 s intervals.

The sensitivity to painful heat stimuli was assessed by recording the paw withdrawal latency with a Hot Plate (52 °C or 30–55 °C surface, Föhr Medical Instruments, Germany) or with the Hargreaves test (IITC Life Science). In the latter, an infrared lamp was placed with a mirror system underneath the respective hind paw. By pressing the start button the lamp starts to emit a heat-beam until the paw is withdrawn, which stops the lamp. The mean paw withdrawal latency of three tests with at least 10 min intervals was used for statistical analysis.

The Orofacial Pain Assessment Device (OPAD, Stoelting, Ireland) allows for evaluation of facial thermal nociception by using a reward-conflict paradigm. The OPAD cage consists of a plexiglas chamber with metal grid floor and an adjustable slit giving access to the nipple of the reward bottle, which is flanked with two PC-controlled thermal peltier elements. To receive the reward (diluted milk in water), the mouse has to touch the thermodes with its cheeks. Hence, the mouse has to decide between receiving a reward or escaping the aversive heat or cold stimulus. Mice were fasted overnight to increase the appetite. Mice were trained three times a week for two weeks at innocuous temperatures (36.5–38 °C) to get a stable baseline of at least 600 licks in 18 min. During test periods, temperature circles starting from neutral (37 °C, 3 min) to aversive cold (15 °C, 10 °C each 3 min) or aversive heat (45 °C, 54 °C each 3 min) were applied using a ramping protocol. Circles were repeated up to 20 min. The ANY-maze software (Version

4.99, Stoelting) registered licks and contacts with the thermodes. The average and total numbers of licks and contacts at the defined temperatures were used for analysis. Ramping times were excluded.

Analysis of olfactory functions

The Novel Odor Recognition Test (NOdorR) was used to assess whether mice were able to detect and differentiate between odors. Mice were habituated to a 3-chambered test box (sizes as for social tests) for 3 days, each for 10 min. The test sessions consisted of three different stages. During (1) habituation, mice were again adapted to the box for 10 min. During (2) "Learning", two petri dishes with perforated lids containing 2 × 2 cm filter papers soaked with identical odors (1% vanilla) were placed in both side chambers. The mouse was placed in the middle and was allowed to explore odors for 10 min. In (3) "Novelty", the settings were identical to the learning stage except that one of the familiar odors (1% vanilla) was replaced with a novel one, which was undiluted rose water. After each test session, the open field was carefully cleaned. Filter papers and petri dishes were freshly prepared for each mouse. Visits of chambers, visits of odors and the time spent with odors were recorded with the VideoMod2 Software. In analogy, odor preferences were tested for urine mixtures of stranger mice.

Analysis of social cognition and memory

The social test apparatus consisted of a rectangular, three-chambered box (42.5 cm wide, 22.2 cm high) with a central chamber 17.8 cm in length and two side chambers each 19.1 cm in length, according to recommended specifications [78]. The central chamber was separated from the side chambers by removable partitions with doors allowing the animal to move freely between chambers. The "stranger" stimulus mouse was positioned in a grid enclosure (Ugo Basile, Italy) allowing close interactions and nose contact but preventing the stranger mouse from initiating social contact. The enclosures had an internal diameter of 7 cm, and height of 15 cm. The top and bottom were constructed from grey PVC.

We used two stimulus mice in each experiment with the same gender and strain as the test mouse, but housed in another room. Mice were habituated to the test box for 3 days, each for 10 min. The sessions were similar as for the NOdorR: (1) Habituation: the animal was placed in the middle chamber with the dividers closed to allow exploration of the middle chamber for 5 min. (2) Sociability test: after the 5-min habituation period, an unfamiliar adult gender-matched mouse (stranger 1) was placed inside the grid enclosure in one of the side chambers. An identical empty grid enclosure was placed in the opposite chamber. The dividers were then raised, allowing the test mouse to move freely among the chambers over a 10-min test session. (3) Novelty: The original stranger mouse (stranger 1) remained in its grid enclosure on one side of the apparatus. A new unfamiliar mouse (stranger 2) was placed in the grid enclosure on the opposite side. The behavior was observed for 10 min. Visits of strangers and the time spent with strangers were recorded. A "visit of stranger" required close proximity of the nose with the grid enclosure with a maximum distance of one cm.

Phenomaster

The TSE Phenomaster offers an automated metabolic and behavioral monitoring in home cage environments. Drinking and feeding behavior were monitored with high-precision weight sensors for liquid and food dispensers, which are integrated into the lid of the cage. Mice were adapted to the drinking bottles for one week in their home cage and to the Phenomaster® cage for 2 consecutive days before starting the experiment. Drinking, feeding and voluntary wheel running were recorded for 24 hours.

Analysis of motor functions

Motor coordination and endurance were assessed with the accelerating RotaRod test (16–32 rpm, ramp 3 rpm/min, cut-off 5 min; Ugo Basile, Italy) or a RotaRod at constant speed. Mice were trained with 2–3 training runs. The running time in test trials was averaged from three trials. The cut-off time was 300 s.

Motor functions of the front limbs were assessed with the mouse staircase test (Campden Instruments Ltd., UK). The test apparatus comprises two compartments, a start compartment with a hinged lid and a test compartment containing a small central platform with two staircases (8 steps) on each side. Each step has a cup for a reward, which was filled with sweet pellets. At the beginning, mice were set on a restriction diet to increase the appetite. Mice were adapted to the sweet rewards for three days in the home cage (d 1–3) and in two training trials (d 5–6). Test sessions were performed at day 7 to 9 and lasted 30 min. Mice were placed into the test compartment, and the behavior to grasp, lift and collect food was monitored with a video camera, and analyzed with VideoMod2. The numbers of pellets remaining on the steps or floor were counted.

Grip strength was assessed with a computerized Grip-Strength Meter (Model 47200, Ugo Basile, Italy). The apparatus consists of a grasping grid connected to a force sensor. To measure the grip strength of front limbs and/or hind limbs, mice were held by the tail and allowed to grasp the grid. As soon as the mouse grasped the grid, the mouse was pulled backwards by the tail until the grip was lost. The peak force of each measurement was automatically recorded in gram-force (gf) by the software. The grip strength was the mean of three trials.

Culture and staining of primary DRG neurons

Primary adult dissociated DRG neuron-enriched cultures were prepared by dissecting mouse dorsal root ganglia (DRGs) into 1x PBS (Phosphate Buffered Saline, Gibco, Germany), followed by digestion with 5 mg/ml collagenase A and 1 mg/ml dispase II (Roche Diagnostics, Germany). Triturated cells were centrifuged through a 15% BSA (bovine serum albumin) solution and plated on poly-L-lysine and laminin coated cover slips in Neurobasal medium (Gibco) containing 2% (vol/vol) B27 supplement (Gibco), 50 µg/ml Pen-Strep, 100 ng/ml NGF and 200 mM L-glutamine. After incubation for 2 h, 2 ml Neurobasal medium was added and neurons were cultured for up to 48 h depending on the experimental requirements. Cells were kept at 37 °C, 5% CO₂, 95% humidity. Primary DRG neurons were used for calcium imaging and immunohistochemistry stainings.

Calcium Imaging

Calcium fluxes were measured fluorometrically as the ratio of the absorbances at 340 and 380 nm (F_{340/380}) in cultured adult DRG neurons (see DRG primary cultures). Calcium-imaging experiments were performed with a Leica calcium-imaging setup, consisting of a Leica DMI 4000 b inverted microscope equipped with a DFC360 FX (CCD) camera, Fura-2 filters, and an N-Plan 10x/0.25 Ph1 objective lens (all from Leica). Images were captured every two seconds and were processed with the LAS AF-software (Leica). Cells were loaded with 5 μ M of the Ca²⁺-sensitive fluorescent dye Fura-2-AM-ester (Biotium), incubated for 40 min at 37 °C and washed three times with ringer solution (Fresenius). Coverslips were then transferred to a perfusion chamber with a flow rate of 1–2 ml/min at room temperature. Baseline ratios were recorded with ringer solution for 100–180 s, before application of either 0.01% formalin to activate TRPA1 or 50 nM capsaicin (Sigma) to activate TRPV1 ion channels for 100 s or 26 s, respectively. After wash-out with ringer solution, cells were perfused with 100 mM KCl (high K⁺) to assess depolarization-evoked calcium currents and the viability of the neurons. Data are presented as changes in fluorescence ratios (F_{340/380}) normalized to baseline ratios. The analysis encompassed 300–350 neurons per condition of 10–12 independent DRG cultures of each three mice per group per stimulus, which were 18 months old. The maximum, the time of maximum and area of the fold increase versus time curve was calculated by integration (Origin Pro 2020 software) with the baseline fixed at Y = 1. The time courses and areas were used for statistical comparison.

Quantitative real-time PCR (QRT-PCR)

Mice were sacrificed via carbon dioxide followed by rapid blood withdrawal. The dorsal root ganglia were rapidly dissected and frozen in liquid nitrogen. Total RNA was extracted from mouse tissue and reversely transcribed with random primers. Twenty nanograms of cDNA equivalent were subjected to quantitative real-time polymerase chain reaction (qRT-PCR). The PCR reaction and amplicon detection were done on a TaqMan (AB 7500 Applied Biosystems; Life Technologies Corporation, Carlsbad, CA) using a FastStart Universal Master Mix (Roche Diagnostics, Mannheim, Germany) with SYBR Green fluorescence staining. TRP channel mRNA were amplified with specific primers and were normalized to the housekeeping gene protein phosphatase 1 (PPP1CA). The comparative threshold cycle (CT) method was used for quantification of relative mRNA expression. The primer pairs are summarized in Suppl. Table 1a.

Immunohistochemistry

Mice were terminally anesthetized with isoflurane and cardially perfused with cold 0.9% NaCl followed by 2% paraformaldehyde (PFA) for fixation. Tissues were excised, postfixed in 2% PFA for 2 h, cryoprotected overnight in 20% sucrose at 4 °C, embedded in small tissue molds in cryo-medium and cut on a cryotome (10 μ m for DRGs and ScN, 12 μ m for SC). Slides were air-dried and stored at – 80 °C. After thawing, slides were immersed and permeabilized in 1xPBS with 0.1% Triton-X-100 (PBST), then blocked with 3% BSA/PBST, subsequently incubated overnight with the first primary antibodies in 1% BSA/PBST at 4 °C. After washing three times with PBS, slides were incubated with the secondary antibodies for 2 h at room temperature, followed by 10 min incubation with DAPI and embedding in Aqua-Poly/Mount. The general settings were optimized for the respective antibodies and tissues. Primary antibodies included STING, IFI16, Tuji, Ceramides, SNCA (Suppl. Table 1b). Secondary antibodies were labeled with fluorochromes

(Invitrogen, Sigma, Life Technologies). Slides were analyzed on an inverted fluorescence microscope (BZ-9000, KEYENCE, Germany and Axio Imager Z1, Zeiss, Germany). Tiled images were obtained to reconstruct whole DRG or spinal cord sections to assess different regions of DRG neurons and fibers.

For analysis of neurite outgrowth and morphology, primary neuron cultures were washed in PBS, fixed in 4% PFA and immunostained with antibodies directed against neurofilament of 200 kDa and subsequent Alexa-488 or Cy3 labeled secondary antibodies, and with phalloidin-Alexa-594. Images were captured on an inverted Axio Imager Z1 fluorescence microscope (Zeiss, Jena, Germany). Tiled images were obtained to reconstruct the whole cultures and assess density of neurons and dendrites.

For quantification, RGB images were converted to binary images using threshold setting implemented in ImageJ with minor adjustments. The particle counter of FIJI ImageJ was used to assess the area covered with neuronal immunoreactive structures.

Transmission electron microscopy

Mice were terminally anaesthetized with carbon dioxide and perfused transcardially with cold 0.9% sodium chloride (NaCl) followed by perfusion with the fixation solution containing 4% PFA and 4% glutaraldehyde in 0.1 M cacodylate buffer, pH 7.4. DRGs were excised and postfixed in the fixation solution for 90 min. After washing 3 times with 0.1 M cacodylate buffer, the tissue was osmicated (1% OsO₄ in 0.1 M cacodylate buffer) for 60 min, washed 3 times with 0.1 M cacodylate buffer and dehydrated in ethanol, 1% uranyl acetate and propylene oxide. The tissue was then incubated in Durcupan resin (Fluka, Durcupan ACM-Kit) overnight and embedded in fresh Durcupan resin at 56 °C for 48 h. Ultrathin sections (54 nm) were cut with a diamond blade, collected on single slot Formvar-coated copper grids and contrasted with lead citrate. Sections were analyzed using a Zeiss electron microscope (Zeiss EM900) and imaged with a slow-scan CCD-Camera.

Oxygraph analysis of mitochondrial OXPHOS activity

Brain sections (prefrontal cortex, hippocampus) and DRG plus trigeminal nerve plus ganglion were immediately transferred into ice-cold Respiration medium MiR06Cr containing 280 U/ml catalase (Pesta&Gnainer, 2012). Tissue was homogenized using a motor-driven tightly fitting glass/Teflon Potter-Elvehjem homogenizer. Mitochondrial respiration was measured using high-resolution respirometry (Oxygraph-2 k, Oroboros Instruments, Innsbruck, Austria) with DatLab software 6.1.0.7 (Oroboros Instruments, Innsbruck, Austria). LEAK-respiration was induced by the addition of complex I –linked substrates pyruvate (5 mM), malate (0.5 mM) and glutamate (10 mM). Complex I – linked respiration was measured after adding ADP (2.5 mM) in a saturating concentration. To measure complex II-linked respiration, rotenone (0.5 μM) was added to block complex I followed by the addition of succinate (10 mM). Maximum uncoupled respiration (ETS, electron transfer system capacity) was measured after stepwise titration of FCCP ((carbonyl cyanide-p-trifluoromethoxyphenylhydrazone). Residual oxygen consumption (ROX) was determined after sequential inhibition of complex III with Antimycin A and complex IV with azide. Absolute respiration rates were corrected for ROX and normalized for the protein content.

Lipid analyses

Sphingolipids and ceramides were analyzed in plasma and in tissue of the spinal cord (SC), dorsal root ganglia (DRG) and sciatic nerves (ScN) of aged Pink1SNCA and wildtype control mice. Lipid analyses were done using liquid chromatography-electrospray ionization-tandem mass spectrometry (LC-ESI-MS/MS), according to procedures described in detail in [79]. The analysis encompassed dehydro-ceramides (Cer d18:0/16:0, Cer d18:0/18:0, Cer d18:0/24:0, Cer d18:0/24:1), ceramides (Cer 18:1/16:0, Cer 18:1/18:0, Cer 18:1/20:0, Cer 18:1/22:0, Cer 18:1/24:0, Cer 18:1/24:1), glucosyl- (GlcCer 16:0) and lactosylceramides (LacCer 18:0, LacCer 24:0, LacCer 24:1), sphinganine (d18:0 SPH, d20:0 SPH), sphingosine (d18:1 SPH) and the respective phospho-SPH's (d18:0 S1P, d18:1 S1P).

In brief, tissue samples were homogenized by adding ethanol:water (1:3, v/v, tissue concentration 0.02 µg/ml) using a ball mill mixer (MM400, Retsch, Haan, Germany) with 4 zirconium oxide grinding balls (25 Hz for 2.5 min). Subsequently, 50 µl of the homogenate were extracted using a liquid-liquid-extraction method. Plasma sample volumes were 10 µl. The quantification of all analytes was performed using a hybrid triple quadrupole-ion trap mass spectrometer QTRAP 5500 (Sciex, Darmstadt, Germany) equipped with a Turbo-V-source operating in positive ESI mode. Sphingolipids were separated using an Agilent 1290 HPLC system equipped with a Zorbax C18 Eclipse Plus UHPLC column (50 Å~ 2.1 mm, 1.8 µm, Agilent technologies, Waldbronn, Germany). Quality control samples of three different concentration levels (low, middle, high) were run as initial and final samples of each run. For all analytes, the concentrations of the calibration standards, quality controls and samples were evaluated by Analyst software 1.6 and MultiQuant Software 3.0 (Sciex) using the internal standard method (isotope-dilution mass spectrometry). Calibration curves were calculated by linear or quadratic regression with 1/x weighting or 1/x² weighting. Variations in accuracy of the calibration standards were less than 15% over the range of calibration, except for the lower limit of quantification (LLOQ), where a variation in accuracy of 20% was accepted. Lipid concentrations in tissue are expressed as pg/mg of the tissue or ng/ml of plasma. For multivariate statistical analyses, lipid data were normalized on the mean value of the respective tissue, and they are expressed as percentages of the mean because the concentrations of different lipids differ by several orders of magnitude.

Statistics

Group data are presented as mean ± SD or mean ± sem, the latter for behavioral time course data, specified in the respective figure legends. Data were analyzed with SPSS 24 and Graphpad Prism 8.0 and Origin Pro 2020. Data were mostly normally distributed, or log-normally distributed. For testing the null-hypothesis that groups were identical, the means of two groups were compared with 2-sided, unpaired Student's t-tests. The Mann Whitney U test was used as a non-parametric alternative in case of violations of t-test requirements. Time course data or multifactorial data were submitted to 2-way analysis of variance (ANOVA) using e.g. the factors 'time' and 'genotype'. In case of significant differences, groups were mutually compared at individual time points using post hoc t-tests according to Dunnett, i.e. versus the control group, or according to Šidák. In case of violations of sphericity, degrees of freedom were

adjusted according to Huynh Feldt. Asterisks in figures show multiplicity-adjusted P-values. The areas under the curve of calcium imaging data were log-normally distributed and were Log₂-transformed for statistical comparisons. The areas were calculated by integration and the distribution was obtained by Kernel density estimation (Origin Pro).

Principal component analysis was used to define the lipid species, which accounted most for the variance between genotypes. Further multivariate analyses included canonical discriminant analysis to assess the predictability of group membership and separation of genotypes and tissues. Partial least square analysis was used if analytes exceeded the number of samples per group. The statistical analysis of RNAseq data is explained below.

RNA sequencing and analysis

DRGs were removed and flash-frozen on dry ice. RNA was harvested using Trizol reagent. Illumina TruSeq RNA Sample Prep Kit (TruSeq Total RNA with Ribo-Zero rRNA depletion) was used with 1 µg of total RNA for the construction of sequencing libraries. Libraries were prepared according to Illumina's instructions. Sequencing was performed with an Illumina Next Generation sequencing system with a sequencing depth of 50 Mio reads per sample.

Sample quality was assessed with demultiplexed fastq.gz files and subsequently the alignment was performed with SeqMan NGen 16 (Lasergene) using the reference genome mm10 provided from UCSC (GRCm38) [80] as template, a minimum read length of 35 bp and automatic adapter trimming. Results were displayed with ArrayStar 16 (Lasergene) including the amount of mapped reads, target length, source length and position, strand, genes and gene IDs, annotated according to the mm10 assembly, and reads were normalized according to RPKM. Alternative DEseq2 normalization yielded equivalent results. Normalized reads were analyzed with ArrayStar, which uses general linear models to assess differential expression. Genes were filtered for at least 10 valid values out of 17 samples with normalized reads > 0.05 to exclude low expression genes. Data were log₂ transformed, single missing values were imputed from the normal distribution, and results were displayed as scatter plots, MA-plots and Volcano plots, the latter showing the log₂ difference i.e. fold change (positive for upregulated genes and negative for downregulated genes) versus the $-\log_{10}$ of the t-test P value. The P value was set at 0.05 and adjusted according to Benjamini Hochberg. Hierarchical clustering was employed to assess gene expression patterns using Euclidean distance metrics. Results were displayed as heat maps with dendrograms.

Key regulated genes (based on P-value, fold change and abundance) were further analyzed for gene ontology annotation enrichments for 'cellular component', 'biological process' and 'molecular function', KEGG, Biocarta and Reactome pathways, SMART domains and SP-PIR-keywords to assess common localizations and functions of significantly regulated genes. GO analyses were done with the "term enrichment" and "functional gene clustering" tools of The Database for Annotation, Visualization and Integrated Discovery (DAVID, version 6.8) (<http://david.abcc.ncifcrf.gov/home.jsp>) [81]. In addition, gene set enrichment analyses (GSEA) (<http://www.gsea-msigdb.org>) [82] were used to further assess functional implications of up- or downregulated genes and to obtain a gene ranking and heat map of the

leading edge 50 up- and downregulated genes. GSEA generates ranked gene lists based on fold difference and P value. The RNAseq data have been deposited as GEO dataset with the provisional accession number GSE146091.

Results

Loss of thermal nociception and of nutritive olfaction in middle-aged Pink1SNCA mice

General health and adequate motor functions are prerequisites to interpret sensory tests, which rely on paw withdrawal or locomotion. During adult life up to middle age (9–10 months of age), Pink1SNCA mice had normal body weight (Fig. 1A), and they behaved normally in most motor function tests including voluntary wheel running, grip strength (Fig. 1A) and distances travelled in mazes. Only in the accelerating Rota Rod, half of the Pink1SNCA mice did not reach the upper target running time of 5 min, whereas all wildtype controls succeeded (Fig. 1A). Hence, voluntary locomotion, which is required for paw withdrawal, is unimpaired at this age.

Pink1SNCA mice had normal paw withdrawal latencies upon mechanical stimulation, but showed a dramatic loss of thermal heat sensitivity in Hargreaves and Hot Plate tests (Fig. 1B), and they had lost the normal warm preference in a Thermal Gradient Ring test, in which mice can freely choose their temperature of well-being (Fig. 1C). The behavior suggests a loss of thermal sensation, which was confirmed for trigeminal hot/cold stimulation in the Orofacial Pain Assessment Device (OPAD), in which mice have to touch heated or cooled metal bars to get access to a rewarding milk bottle. Pink1SNCA had more contacts and more licks at unpleasant hot or cold temperatures suggesting that they did not feel the unpleasantness (Fig. 1D).

In the Novel Odor Recognition and memory test, Pink1SNCA mice were less interested in the pleasant odors vanilla or rose than wildtype control mice, and they did not reach out to the sweet pellets presented on the steps of a staircase test, suggesting a loss of olfactory sensitivity (Fig. 1E). However, they maintained a stronger appeal to vanilla than rose like the controls suggesting that they were able to discriminate between odors (Fig. 1E).

Repetition of the odor recognition test with social odors (urine mixtures) yielded different results. Pink1SNCA responded equally to the social odor and were more interested in the novel odor relative to the familiar one in the second phase of the test (Fig. 1F). Sensation and processing of pleasant odors in mice requires dopaminergic neurons of the olfactory bulb, which are a primary site PD pathology, whereas social odors depend on neurons of the vomeronasal organs and accessory olfactory bulb [39], which are likely less affected in PD mice. Social behavior is therefore preserved. In confirmation, social contacts with familiar or stranger mice in the sociability test were normal in Pink1SNCA mice (Fig. 1G). Analyses of the total distances travelled in the maze tests revealed that Pink1SNCA mice were overactive in social tests or social environments (Fig. 1H).

Onset of premotor sensory loss

Nociceptive tests were repeated in younger mice to assess the onset of thermal sensory losses. There were no differences at 2 months of age but the first significant protraction of paw withdrawal upon heat stimulation occurred at 4 months of age (Fig. 2A), hence 11 months before the earliest occurrence of spontaneous motor deficits. Motor function Rota Rod tests at 4 months were not impaired, but some Pink1SNCA mice needed more trials to achieve the running goal of 300 s, whereas all wildtype controls succeed on the first or second training run (Fig. 2A).

There was no sensory loss in single mutant mice at 9–10 months of age but rather nociceptive hypersensitivity for mechanical stimuli in Pink1^{-/-} mice, or heat stimuli in SNCA A53T mice, suggesting a progression from hypersensitivity to sensory loss with the number of molecular defects.

RNA sequencing reveals loss of acidic fibroblast growth factor in the DRGs

The behavior of Pink1SNCA mice shows a prodromal loss of thermal somatosensation, which may be caused by a predominant loss of sensory neurons with unmyelinated C-fibers, or a specific downregulation of ion channels, which contribute to the sensation of heat and cold. In search of putative mechanisms, we performed gene expression analyses by RNA sequencing in DRG tissue of prodromal middle-aged to old mice (Fig. 3). Clustering of mice for the 1000 top regulated genes (at 90% confidence level with 1.5fold change) perfectly separated Pink1SNCA from wildtype mice. Apart from the knockout of Pink1, a prominent down-regulated gene was acidic fibroblast growth factor, Fgf1 (Fig. 3B, C), which is known to restore the survival of dopaminergic neurons in PD models [40, 41] and contributes to neurogenesis [42]. Up-regulated genes included DNase1l3, CCL27 and CCL25, IFI44 and IL31ra, and pointed to increased DNase activity and activation of the immune system.

Gene ontology analyses agreed with the top candidates. The major terms, which were enriched in downregulated genes (top 200) were "proteolysis", "cell differentiation", and the cellular compartment, "transmembrane". Major terms in upregulated genes were "nuclease", "lipid metabolism", "ion channel/ion transport" and "chemotaxis/immune response". GSEA gene set enrichment analysis agrees with these top GO terms, in particular a negative enrichment of "Notch signaling" (Hallmark gene sets), "axon guidance" (Reactome gene sets) or "focal adhesion" (KEGG gene sets). Leading edge genes according to GSEA are shown in Suppl. Figure 1 and selected pathways in Suppl. Figure 2

Hence, from the behavioral studies with loss of thermal sensation and from the RNAseq studies with prominent deregulations of Fgf1, ion channels, innate immune genes and DNase we decided to follow up on key aspects that may ultimately lead to thermal sensory loss, i.e. TRP channel dysfunction, sphingolipid metabolism, mitochondrial dysfunction and DNA triggered innate immune responses. The RNAseq data have been deposited as GEO dataset with the provisional accession number GSE146091.

Loss of TRP-channel dependent calcium fluxes in sensory neurons of the DRGs

The behavioral results pointed to a specific early-onset loss of thermal sensation, agreeing well with results of Quantitative Sensory Tests in sporadic PD patients, where the predominant QST phenotype is thermal sensory loss plus mechanical hypersensitivity. Thermal sensitivity relies on the expression and functioning of TRP channels, mainly TRPVs for heat, and TRPA1 and TRPMs for cold.

To assess functions of these TRP channels, primary DRG neurons of 18 months old Pink1SNCA and wildtype mice were stimulated with capsaicin to activate TRPV1 and formalin to activate TRPA1. Calcium influx was determined as Fura2 absorbance ratios from 300–350 neurons per group and stimulus. High-K⁺ responsive neurons (80–90% in each culture) were used for group comparisons (Fig. 4). Time courses of $[Ca^{2+}]_i$ and violin plots of the areas under the curve (AUC) revealed lower peak calcium influx and reduced net increases upon stimulation irrespective of the stimulus (Fig. 4A-D). DRG neurons of Pink1SNCA mice were more heterogeneous than WT neurons and showed a triple-phasic distribution upon stimulation with capsaicin or formalin representing non-responding, low-responding and high-responding neurons. Similarly, a double peak distribution upon High-K⁺ stimulation contrasted the monophasic distribution of the wildtype neurons, and revealed that about half of the Pink1SNCA neurons had lower depolarization-evoked calcium raises. The morphology of primary DRG neuron cultures, neurite outgrowth and immunofluorescence analyses of markers of autophagy and protein aggregates did not differ between genotypes (Suppl. Figure 3). Hence, the changes of excitability were not caused by neuronal death.

Immunofluorescence analyses of TRPV1 in DRGs showed a reduction of TRPV1-immunoreactive neurons in DRGs of Pink1SNCA mice (Fig. 4E, quantification 4F), which was confirmed at RNA level via rt-PCR for TRPV1 and TRPA1 (Fig. 4G). The RNA profile of various TRP channels obtained via RNAseq showed a reduction of TRPVs and TRPA1, and increase of TRPMs, whereas TRPCs were mostly unaffected (Fig. 4H). The gene expression analyses agree with the calcium imaging results.

Immunofluorescence studies of DRGs with neuronal markers and markers of autophagy and apoptosis did not reveal overt differences of autophagy or neuronal death (Suppl. Figure 4), suggesting that the observed alterations of specific ion channels were not the consequence of neuronal loss. Indeed, there were no differences of gene expression of voltage-gated calcium or sodium channels, but a number of subunits of voltage-gated potassium channels were increased (Suppl. Figure 2A), which regulate the excitability of somatosensory neurons [43] and responsiveness of TRP channels [44]. Biogenic amine receptors and transporters were in part deregulated (Suppl. Figure 2B), whereas mitophagy/autophagy marker were mostly unaffected (Suppl. Figure 2C), except Pink1 itself.

Accumulation of glucosylceramides in DRGs and loss of sphingolipids in the sciatic nerve

We have previously shown that ceramides accumulate progressively in the olfactory bulb of *Pink1*^{-/-} single mutant mice [45], and glucosylceramides altered the responsiveness of TRP channels [46], suggesting that alterations of sphingolipids contribute to PD-associated sensory dysfunctions.

To address this aspect, sphingolipids of different classes were analyzed in DRGs, sciatic nerve (ScN), spinal cord (SC) and plasma from 12 months old *Pink1*^{SNCA} and wildtype control mice (n = 8 per group). The analysis encompassed dehydro-ceramides, ceramides, glucosyl- and lactosylceramides, as well as sphinganine, sphingosine and the respective phospho-SPH's. Plasma levels did not differ between groups (not shown), but there were substantial differences in tissue levels, which mostly originated from DRGs and ScN. Discriminant Principal Component Analysis using the lipids in DRGs and ScN as input revealed that GluCer16:0 (increased), the SPH's (decreased) and LacCer24:1 (decreased) accounted for most of the variance between groups. Based on PC1 and PC2, groups were clearly separated (Fig. 5A). Scatter 3D plots of key lipids with all tissues (i.e. also including spinal cord) show some overlap of 95% CI ellipsoids (mainly caused by SC) but still separate groups (Fig. 5B). Further pairs were compared in a scatter matrix (Suppl. Figure 5A) and reveal a clear group separation based on GluCer16:0 versus either sphinganine or sphinganine-1-phosphate. Canonical Discriminant analysis shows the tissue specific group separations (Suppl. Figure 5B). Polar plots showing the mean of normalized lipids as percentages (relative to the mean of all mice set to 100%) reveal the tissue specific patterns of sphingolipid alterations (Fig. 5C, Suppl. Figure 5C). In the DRGs, the accumulation of ceramides is prominent whereas loss of sphingosines and sphinganine predominates in the sciatic nerve. The spinal cord is not affected. The increase of ceramides was also detected in DRG neurons of aged mice (Fig. 4D). Tissue specific concentrations and ANOVA statistics of lipids are shown in Fig. 6.

Accumulation of GlcCer and lower levels of LacCer in the DRGs suggest that the lysosomal metabolism of GlcCer via glucocerebrosides (GBA1) to LacCer is impaired, which would agree with associations of GBA1 dysfunctions with PD [28], and with increased alpha synuclein toxicity in the presence of GBA1 mutations [27, 29, 47]. Gene expression analysis (RNAseq) in the DRGs of our mice did not reveal lower GBA1 transcription (Suppl. Figure 2D). Instead, low ceramidase (*Asah2*) and increases of *Cers4* (ceramide synthase), *Degs1* (sphingolipid desaturase) and *Smpd5* (sphingomyelin phosphodiesterase) suggest a combination of lower ceramide breakdown and increased formation.

Reduction of oxygen consumption of sensory neurons pointing to mitochondrial defects

Intracellular accumulation of GlcCer owing to GBA1 mutations are supposed to interfere with mitochondrial functions and autophagolysosomal removal of damaged mitochondria via mitophagy [48, 49]. Using oxygraph respirometry, we measured cellular oxygen consumption and OXPHOS activity with 'substrate-uncoupler-inhibitor' titration protocols in freshly prepared tissue of the prefrontal cortex, hippocampus and of sensory ganglia (DRGs and trigeminal ganglia) in 18 months old *Pink1*^{SNCA} versus wildtype control mice (Fig. 7A exemplary respirograms and 7B quantification). There were no differences between genotypes in the brain, but oxygen consumption and Complex I and Complex II activity were

significantly reduced in sensory ganglia of Pink1SNCA mice. There were no differences in citrate synthase activity at any site (Suppl. Figure 5D).

The ultrastructural morphology of dark neuronal mitochondria (crista type) in the DRGs of 16 months old mice was alike in Pink1SNCA and wildtype control mice (Fig. 8). There were also no other overt differences in terms of cellularity, neuronal morphology, myelin sheaths or vascular cells (Fig. 8). The DRG neurons displayed a high number of autophagolysosomes, which were present in similar numbers in both genotypes, and also occur in DRGs of younger mice [50].

However, there was a higher proportion of neurons highly packed with white very prominent mitochondria in Pink1SNCA DRGs (overview upper panel in Fig. 8), which do not normally occur in the DRGs of younger mice [50]. The frequency of neurons with such mitochondria was 0-3.5% in sections of WT DRGs and 6–15% in Pink1SNCA DRGs. These white mitochondria in part gave a swollen impression and had lost or disorganized cisternae. Similar changes of mitochondrial morphology have been previously described in neurons of the cortex and substantia nigra of Parkin-SNCA double mutant mice [51].

Increase of innate immune markers in the DRGs

It has been suggested that mitochondrial damage in combination with defective mitophagy results in deposits of mitochondrial DNA (mtDNA) in the cytosol which triggers a cGAS-cGAMP-STING (cGAMP = cyclic guanosine monophosphate adenosine monophosphate, cGAS = cGAMP synthase) mediated innate immune response leading to increases of interferon regulated genes [52–55]. It was shown that mtDNA-evoked inflammation in Pink1 deficient mice could be rescued by concurrent loss of STING [56]. Hence, considering the observed mitochondrial dysfunctions and deregulations of innate immune pathways we assessed the key candidates, which showed differential gene expression in RNAseq experiments, IFI16/IFI204 and STING (Fig. 9). The immunofluorescence of IFI16/IFI204 suggests a stronger distribution of IFI16 in the cytosol in Pink1SNCA mice (Fig. 9A), and RNAseq shows a decrease of its RNA (Fig. 9B). The immunofluorescence of STING did not show overt differences (Fig. 9A), but at RNAseq level, STING expression was increased (Fig. 9B). Analysis of multiple interferon-stimulated genes (Fig. 9B) and of chemokines (Suppl. Figure 2E) would agree with a stimulation of innate immune pathways.

Discussion

Sensory neuropathies occur in PD with higher frequency than in age-matched control subjects, and the onset is often years before the occurrence of motor dysfunctions [16]. The high vulnerability of the sensory neurons may result from their anatomy, in particular very long axons requiring organelle transport over long distances and exposure to peripheral environments, but the pathophysiology is not well understood. In contrast to olfactory sensory neurons, which are also affected early in the course of PD, only few neurons of the dorsal root ganglia express marker of dopaminergic neurons [57].

We show in the present study that Pink1SNCA double mutant mice phenocopy the prodromal sensory neuropathy. They develop a progressive loss of thermal sensation far earlier than the earliest occurrence of clinical motor dysfunctions. The sensory phenotype is reminiscent of QST phenotypes of PD patients, which presents with a predominant loss of thermal sensation and preservation of mechanical sensitivity or mechanical hypersensitivity [18, 58]. Pink1SNCA mice replicate the thermal versus mechanical dichotomy. Thermal sensation relies on TRPV1 positive DRG neurons [59, 60], and heat nociception is conveyed mainly through non-myelinated C-fibers [61], suggesting that this population is particularly vulnerable. However, DRG neurons are highly diverse with functional overlap, and the behavioral readouts do not clearly distinguish the most affected subpopulation.

Morphologically, we did not detect overt signs of neuronal death or damage in DRGs of Pink1SNCA mice, but it has been shown that the density of sensory fiber terminals in the skin is reduced in PD patients [15, 58], which is not a specific observation for PD associated sensory neuropathies but occurs frequently in sensory neuropathies associated with metabolic diseases such as diabetes mellitus [62]. The similarities suggests that metabolic dysfunctions of sensory neurons, which are not or not yet visible at the morphological level are important determinants of the sensory decline in PD. In addition, subsets of neurons displayed high numbers of white mitochondria that do not normally occur at younger age and appeared to be swollen with partially disrupted cristae. Such morphological abnormalities bear some resemblance to those described in human PD patients [63–65]. Mitochondria are susceptible to morphological artefacts such as swollen appearance that are caused by inadequate fixation, but occur to some extent with any fixation technique. However, we did not observe swollen mitochondria in DRGs in younger mice in a previous technically identical study [50], and swollen mitochondria were consistently more abundant in Pink1SNCA mice than in controls although the tissue was prepared in parallel (three per genotype). In addition, the morphology agreed with the functional loss of mitochondrial respiration and support the view of a mitochondria-dependent damage in PD neurons.

We have observed in PD patients that sensory loss as assessed by QST measurements and pain intensity ratings are associated with high levels of plasma glucosylceramides. We show in the present study that these glucosylceramides are increased in the DRGs of Pink1SNCA mice strengthening the idea that they contribute to the pathology of sensory neurons. Mutations of GBA1, the key lysosomal enzyme catalyzing GlcCer degradation, have been associated with autophagolysosomal dysfunctions [66, 67], increased alpha-synuclein toxicity [27, 68] and disruptions of mitochondrial energy production [49]. GBA1 expression was unaltered in the DRGs of Pink1SNCA mice, and the ultrastructural morphology of lysosomes and lipid droplets in DRG neurons appeared to be normal for the age. Instead, gene expression analysis suggested that sphingomyelin degradation converging on GlcCer generation was increased, which would agree with the loss of sphingamines and sphingosines in the sciatic nerve and in DRGs, and points to alterations or myelination. The data suggest that GlcCer may accumulate even in the absence of GBA1 defects, which agrees with previous observations in humans [33, 34]. Hence, sphingolipid allostasis in PD may have a broader clinical relevance for PD pathophysiology, not restricted to GBA1 mutation carriers.

We showed previously that GlcCer has dual effects on sensory neurons. It increased the fraction of non-responding neurons on stimulation, but augmented the capsaicin-evoked calcium influx in responsive neurons (accompanying manuscript). The duality reflected the clinical phenotype where sensory loss is often associated with burning pain. It is not clear, if and how GlcCer affect ion channel properties. So far, most studies addressing the functional consequences of GBA1 deletion assumed that the observed pathology was caused by glucosylceramides without directly measuring these lipids. GBA1 deletion or mutation increased alpha-synuclein aggregates [26, 27], led to mitochondrial calcium overload [49], ER stress [69] and disruption of autophagolysosomal pathways [67].

TRP channels are regulated by phosphorylation, redox modification, calmodulin and membrane insertion [70–75]. The ceramide nature of GlcCer suggests that membrane insertion or lipid raft function may be affected [46], ultimately leading to degradation and downregulation of TRPV1, which would agree with the immunofluorescence and gene expression analyses of the DRGs in Pink1SNCA mice. The very early behavioral onset of declining heat sensitivity in Pink1SNCA mice suggest that assessment of warm detection thresholds may qualify as early diagnostic tool.

To stop progression of neurodegeneration one would like to know the causal chain of pathophysiologic events. From the genetics of Pink1SNCA mice, one would assume that defective mitochondria trigger subsequent dysfunctions. Indeed, mitochondrial respiration was reduced, and there was a higher proportion of cells in the DRGs with white mitochondria, which gave a swollen impression. Defective mitophagy owing to Pink1 deficiency is supposed to lead to incomplete removal of damaged mitochondria and may result in a cytosolic mtDNA driven activation of innate immune responses via the cGAS-STING pathway [56, 76, 77]. Previous brain microarray studies from aging Pink1SNCA mice had suggested progressive innate immune pathway dysregulations [45]. However, in the DRGs, sciatic nerve and spinal cord we did not observe invasion with inflammatory cells or satellite cell activation, although STING itself, IFI44l, Irf6 and Irf7 and the chemokines CCL27 and 25 were upregulated at RNA level. Hence, the immune aspect was subtle, although it was in agreement with previous observations, and rather does not explain the sensory loss.

Conclusion

In summary, we show that Pink1SNCA double mutant mice phenocopy the prodromal PD-associated sensory neuropathy, which often precedes motor manifestations for years and poses substantial strain to patients, particularly if it causes chronic pain and is mis-diagnosed owing to the lack of motor impairments. The mice develop a progressive loss of thermal sensation far earlier than the earliest occurrence of clinical motor dysfunctions. We have evaluated multiple mechanistic aspects, which theoretically contribute to the prodromal sensory loss in Pink1SNCA mice. There is no single gene or pathway acting as single originator. However overall, the deregulations of sphingolipid metabolism and (likely consequent) TRP channel disappearances and mitochondrial damage were most convincing to explain the behavioral phenomena of early prodromal somatosensory loss and suggest that sphingolipid metabolic pathways pose novel therapeutic options.

Abbreviations

DRG, dorsal root ganglia; Fgf1, acidic fibroblast growth factor; cGAS, cyclic GMP-AMP Synthase; GBA1, Glucocerebrosidase beta (alias glucosylceramidase); IFI16, gamma-interferon-inducible protein; mtDNA, mitochondrial DNA; dhCer, dehydro-ceramide; GlcCer, Glucosylceramides, SPH, sphingolipids; dhSPH, dehydro-sphingolipid; PD, Parkinson's Disease, QST, Quantitative Sensory Testing; Pink1, PTEN inducible kinase 1; SNCA, alpha-synuclein; STING, Stimulator of Interferon Genes; TRPV1, Transient Receptor Potential Channel class V, member 1; WT, wildtype;

Declarations

Consent for publication

Does not apply

Availability of supporting data

RNAsequencing data have been deposited at GEO datasets with the provisional accession GSE146091.

Reviewer can access the data at

<https://www.ncbi.nlm.nih.gov/geo/query/acc.cgi?acc=GSE146091>

using the Reviewer TOKEN: uzuraakitlmhjgd

Other supporting data are included as Supplementary Files.

Competing Interests

The authors declare that there are no conflicts of interest. The funding institution had no role in data acquisition, analysis or decision to publish the results.

Funding

The study was supported by the Deutsche Forschungsgemeinschaft CRC1039 (A03 to IT; Z1 to GG), CRC1080 (A03 to IT, B03 to TD), SFB815 (A12 to IT; A08 to BB; Z1 to JH) and by the Fraunhofer Cluster of Excellence for immune mediated diseases (CIMD, to GG).

Author contributions

LV performed the behavioral studies, immunofluorescence and EM analyses with tissues and primary cultures, calcium imaging experiments and analyzed data. BT performed behavioral studies. AWS did the RNAseq experiments and organized mice. JH performed the mitochondrial function tests. TS and BB provided assistance of RNAseq experiments. GA generated the Pink1SNCA double mutant mice and discussed data. ST analyzed lipids by LC-MS/MS, and DT and GG organized and managed the lipid

analysis lab. TD provided EM knowledge and discussed data. IT initiated the study, supervised the studies, analyzed calcium imaging, immunofluorescence and omics data, drafted the manuscript and made the figures. All authors contributed to drafting or editing of parts of the manuscript and approved the final version of the manuscript.

Acknowledgement

We thank Anke Biczysko for excellent technical assistance in ultrastructural analyses.

Ethical approval

The experiments were approved by the local Ethics Committee for animal research (Darmstadt, Germany), adhered to the guidelines for pain research in conscious animals of the International Association for the Study of PAIN (IASP) and those of the Society of Laboratory Animals (GV-SOLAS) and were in line with the European and German regulations for animal research.

Authors' information

All authors read and approved the final manuscript.

References

1. Darweesh SK, Verlinden VJ, Stricker BH, Hofman A, Koudstaal PJ, Ikram MA: Trajectories of prediagnostic functioning in Parkinson's disease. *Brain* 2017, 140:429-441.
2. Braak H, Braak E, Yilmazer D, Schultz C, de Vos RA, Jansen EN: Nigral and extranigral pathology in Parkinson's disease. *J Neural Transm Suppl* 1995, 46:15-31.
3. Schrag A, Horsfall L, Walters K, Noyce A, Petersen I: Prediagnostic presentations of Parkinson's disease in primary care: a case-control study. *Lancet Neurol* 2015, 14:57-64.
4. Rana AQ, Siddiqui I, Mosabbir A, Athar A, Syed O, Jesudasan M, Hafez K: Association of pain, Parkinson's disease, and restless legs syndrome. *J Neurol Sci* 2013, 327:32-34.
5. Berardelli A, Wenning GK, Antonini A, Berg D, Bloem BR, Bonifati V, Brooks D, Burn DJ, Colosimo C, Fanciulli A, et al: EFNS/MDS-ES/ENS [corrected] recommendations for the diagnosis of Parkinson's disease. *Eur J Neurol* 2013, 20:16-34.
6. Postuma RB, Aarsland D, Barone P, Burn DJ, Hawkes CH, Oertel W, Ziemssen T: Identifying prodromal Parkinson's disease: pre-motor disorders in Parkinson's disease. *Mov Disord* 2012, 27:617-626.
7. Snider SR, Fahn S, Isgreen WP, Cote LJ: Primary sensory symptoms in parkinsonism. *Neurology* 1976, 26:423-429.
8. Djaldetti R, Yust-Katz S, Kolianov V, Melamed E, Dabby R: The effect of duloxetine on primary pain symptoms in Parkinson disease. *Clin Neuropharmacol* 2007, 30:201-205.
9. Djaldetti R, Shifrin A, Rogowski Z, Sprecher E, Melamed E, Yarnitsky D: Quantitative measurement of pain sensation in patients with Parkinson disease. *Neurology* 2004, 62:2171-2175.

10. Yust-Katz S, HersHKovitz R, Gurevich T, Djaldetti R: Pain in ExtrapYramidal Neurodegenerative Diseases. *Clin J Pain* 2017, 33:635-639.
11. Leclair-Visonneau L, Magy L, Volteau C, Clairembault T, Le Dily S, Preterre C, Peyre A, Damier P, Neunlist M, Pereon Y, Derkinderen P: Heterogeneous pattern of autonomic dysfunction in Parkinson's disease. *J Neurol* 2018, 265:933-941.
12. Zambito Marsala S, Tinazzi M, Vitaliani R, Recchia S, Fabris F, Marchini C, Fiaschi A, Moretto G, Giometto B, Macerollo A, Defazio G: Spontaneous pain, pain threshold, and pain tolerance in Parkinson's disease. *J Neurol* 2011, 258:627-633.
13. Pont-Sunyer C, Hotter A, Gaig C, Seppi K, Compta Y, Katzenschlager R, Mas N, Hofeneder D, Brucke T, Bayes A, et al: The onset of nonmotor symptoms in Parkinson's disease (the ONSET PD study). *Mov Disord* 2015, 30:229-237. doi: 210.1002/mds.26077. Epub 22014 Dec 26071.
14. Kass-Iliyya L, Javed S, Gosal D, Kobylecki C, Marshall A, Petropoulos IN, Ponirakis G, Tavakoli M, Ferdousi M, Chaudhuri KR, Jeziorska M, Malik RA, Silverdale MA: Small fiber neuropathy in Parkinson's disease: A clinical, pathological and corneal confocal microscopy study. *Parkinsonism Relat Disord* 2015, 21:1454-1460. doi: 1410.1016/j.parkreldis.2015.1410.1019. Epub 2015 Nov 1453.
15. Nolano M, Provitera V, Estraneo A, Selim MM, Caporaso G, Stancanelli A, Saltalamacchia AM, Lanzillo B, Santoro L: Sensory deficit in Parkinson's disease: evidence of a cutaneous denervation. *Brain* 2008, 131:1903-1911.
16. Zis P, Grunewald RA, Chaudhuri RK, Hadjivassiliou M: Peripheral neuropathy in idiopathic Parkinson's disease: A systematic review. *J Neurol Sci* 2017, 378:204-209.
17. Nolano M, Provitera V, Manganelli F, Iodice R, Stancanelli A, Caporaso G, Saltalamacchia A, Califano F, Lanzillo B, Picillo M, Barone P, Santoro L: Loss of cutaneous large and small fibers in naive and l-dopa-treated PD patients. *Neurology* 2017.
18. Strobel AV, Tankisi H, Finnerup NB, Fuglsang-Frederiksen A, Jennum P, Svendsen KB, Kirov FI, Otto M: Somatosensory function is impaired in patients with idiopathic REM sleep behaviour disorder. *Sleep Med* 2018, 42:83-89.
19. Silverdale MA, Kobylecki C, Kass-Iliyya L, Martinez-Martin P, Lawton M, Cotterill S, Chaudhuri KR, Morris H, Baig F, Williams N, Hubbard L, Hu MT, Grosset DG: A detailed clinical study of pain in 1957 participants with early/moderate Parkinson's disease. *Parkinsonism Relat Disord* 2018, 56:27-32.
20. Rey NL, Steiner JA, Maroof N, Luk KC, Madaj Z, Trojanowski JQ, Lee VM, Brundin P: Widespread transneuronal propagation of alpha-synucleinopathy triggered in olfactory bulb mimics prodromal Parkinson's disease. *J Exp Med* 2016, 213:1759-1778.
21. Bernis ME, Babila JT, Breid S, Wusten KA, Wullner U, Tamguney G: Prion-like propagation of human brain-derived alpha-synuclein in transgenic mice expressing human wild-type alpha-synuclein. *Acta neuropathologica communications* 2015, 3:75.
22. Loria F, Vargas JY, Bousset L, Syan S, Salles A, Melki R, Zurzolo C: alpha-Synuclein transfer between neurons and astrocytes indicates that astrocytes play a role in degradation rather than in spreading. *Acta Neuropathol* 2017, 134:789-808.

23. Peelaerts W, Bousset L, Van der Perren A, Moskalyuk A, Pulizzi R, Giugliano M, Van den Haute C, Melki R, Baekelandt V: alpha-Synuclein strains cause distinct synucleinopathies after local and systemic administration. *Nature* 2015, 522:340-344.
24. Blanz J, Saftig P: Parkinson's disease: acid-glucocerebrosidase activity and alpha-synuclein clearance. *J Neurochem* 2016, 139 Suppl 1:198-215.
25. Suzuki M, Sango K, Wada K, Nagai Y: Pathological role of lipid interaction with alpha-synuclein in Parkinson's disease. *Neurochem Int* 2018, 119:97-106.
26. Kim S, Yun SP, Lee S, Umanah GE, Bandaru VVR, Yin X, Rhee P, Karuppagounder SS, Kwon SH, Lee H, et al: GBA1 deficiency negatively affects physiological alpha-synuclein tetramers and related multimers. *Proc Natl Acad Sci U S A* 2018, 115:798-803. doi: 710.1073/pnas.1700465115. Epub 1700462018 Jan 1700465118.
27. Zunke F, Moise AC, Belur NR, Gelyana E, Stojkowska I, Dzaferbegovic H, Toker NJ, Jeon S, Fredriksen K, Mazzulli JR: Reversible Conformational Conversion of alpha-Synuclein into Toxic Assemblies by Glucosylceramide. *Neuron* 2018, 97:92-107.e110.
28. Murphy KE, Gysbers AM, Abbott SK, Tayebi N, Kim WS, Sidransky E, Cooper A, Garner B, Halliday GM: Reduced glucocerebrosidase is associated with increased alpha-synuclein in sporadic Parkinson's disease. *Brain* 2014, 137:834-848.
29. Tayebi N, Parisiadou L, Berhe B, Gonzalez AN, Serra-Vinardell J, Tamargo RJ, Maniwang E, Sorrentino Z, Fujiwara H, Grey RJ, et al: Glucocerebrosidase haploinsufficiency in A53T alpha-synuclein mice impacts disease onset and course. *Mol Genet Metab* 2017, 122:198-208.
30. Suzuki M, Fujikake N, Takeuchi T, Kohyama-Koganeya A, Nakajima K, Hirabayashi Y, Wada K, Nagai Y: Glucocerebrosidase deficiency accelerates the accumulation of proteinase K-resistant alpha-synuclein and aggravates neurodegeneration in a Drosophila model of Parkinson's disease. *Hum Mol Genet* 2015, 24:6675-6686.
31. Abul Khair SB, Dhanushkodi NR, Ardah MT, Chen W, Yang Y, Haque ME: Silencing of Glucocerebrosidase Gene in Drosophila Enhances the Aggregation of Parkinson's Disease Associated alpha-Synuclein Mutant A53T and Affects Locomotor Activity. *Front Neurosci* 2018, 12:81.
32. Migdalska-Richards A, Wegrzynowicz M, Rusconi R, Deangeli G, Di Monte DA, Spillantini MG, Schapira AHV: The L444P Gba1 mutation enhances alpha-synuclein induced loss of nigral dopaminergic neurons in mice. *Brain* 2017, 140:2706-2721.
33. Alcalay RN, Levy OA, Waters CC, Fahn S, Ford B, Kuo SH, Mazzoni P, Pauciulo MW, Nichols WC, Gan-Or Z, et al: Glucocerebrosidase activity in Parkinson's disease with and without GBA mutations. *Brain* 2015, 138:2648-2658. doi: 2610.1093/brain/awv2179. Epub 2015 Jun 2627.
34. Murphy KE, Halliday GM: Glucocerebrosidase deficits in sporadic Parkinson disease. *Autophagy* 2014, 10:1350-1351.
35. Robak LA, Jansen IE, van Rooij J, Uitterlinden AG, Kraaij R, Jankovic J, Heutink P, Shulman JM: Excessive burden of lysosomal storage disorder gene variants in Parkinson's disease. *Brain* 2017,

140:3191-3203.

36. Perez-Lloret S, Rey MV, Dellapina E, Pellaprat J, Brefel-Courbon C, Rascol O: Emerging analgesic drugs for Parkinson's disease. *Expert Opin Emerg Drugs* 2012, 17:157-171.
37. Sophie M, Ford B: Management of pain in Parkinson's disease. *CNS Drugs* 2012, 26:937-948.
38. Valek L, Auburger G, Tegeder I: Sensory neuropathy and nociception in rodent models of Parkinson's disease. *Dis Model Mech* 2019, 12.
39. Luo M, Fee MS, Katz LC: Encoding pheromonal signals in the accessory olfactory bulb of behaving mice. *Science* 2003, 299:1196-1201.
40. Wei X, He S, Wang Z, Wu J, Zhang J, Cheng Y, Yang J, Xu X, Chen Z, Ye J, Chen L, Lin L, Xiao J: Fibroblast growth factor 1 attenuates 6-hydroxydopamine-induced neurotoxicity: an in vitro and in vivo investigation in experimental models of parkinson's disease. *Am J Transl Res* 2014, 6:664-677.
41. de Yebenes JG, Pernaute RS, Garrido JM, Rabano A, Albusua J, Rojo A, Mena MA, Ruiz PG, Jorge P, Correa C, et al: Long-term intracerebral infusion of fibroblast growth factors restores motility and enhances F-DOPA uptake in parkinsonian monkeys. *Parkinsonism Relat Disord* 1998, 4:147-158.
42. Ma DK, Ponnusamy K, Song MR, Ming GL, Song H: Molecular genetic analysis of FGFR1 signalling reveals distinct roles of MAPK and PLCgamma1 activation for self-renewal of adult neural stem cells. *Mol Brain* 2009, 2:16.
43. Zheng Y, Liu P, Bai L, Trimmer JS, Bean BP, Ginty DD: Deep Sequencing of Somatosensory Neurons Reveals Molecular Determinants of Intrinsic Physiological Properties. *Neuron* 2019, 103:598-616.e597.
44. Memon T, Chase K, Leavitt LS, Olivera BM, Teichert RW: TRPA1 expression levels and excitability brake by K(V) channels influence cold sensitivity of TRPA1-expressing neurons. *Neuroscience* 2017, 353:76-86.
45. Torres-Odio S, Key J, Hoepken HH, Canet-Pons J, Valek L, Roller B, Walter M, Morales-Gordo B, Meierhofer D, Harter PN, Mittelbronn M, Tegeder I, Gispert S, Auburger G: Progression of pathology in PINK1-deficient mouse brain from splicing via ubiquitination, ER stress, and mitophagy changes to neuroinflammation. *J Neuroinflammation* 2017, 14:154.
46. Santha P, Oszlacs O, Dux M, Dobos I, Jancso G: Inhibition of glucosylceramide synthase reversibly decreases the capsaicin-induced activation and TRPV1 expression of cultured dorsal root ganglion neurons. *Pain* 2010, 150:103-112.
47. Gundner AL, Duran-Pacheco G, Zimmermann S, Ruf I, Moors T, Baumann K, Jagasia R, van de Berg WDJ, Kremer T: Path mediation analysis reveals GBA impacts Lewy body disease status by increasing alpha-synuclein levels. *Neurobiol Dis* 2019, 121:205-213.
48. Li H, Ham A, Ma TC, Kuo SH, Kanter E, Kim D, Ko HS, Quan Y, Sardi SP, Li A, Arancio O, Kang UJ, Sulzer D, Tang G: Mitochondrial dysfunction and mitophagy defect triggered by heterozygous GBA mutations. *Autophagy* 2019, 15:113-130.
49. Plotegher N, Perocheau D, Ferrazza R, Massaro G, Bhosale G, Zambon F, Rahim AA, Guella G, Waddington SN, Szabadkai G, Duchon MR: Impaired cellular bioenergetics caused by GBA1 depletion

- sensitizes neurons to calcium overload. *Cell Death Differ* 2019.
50. Altmann C, Hardt S, Fischer C, Heidler J, Lim HY, Haussler A, Albuquerque B, Zimmer B, Moser C, Behrends C, et al: Progranulin overexpression in sensory neurons attenuates neuropathic pain in mice: Role of autophagy. *Neurobiol Dis* 2016, 96:294-311.
 51. Stichel CC, Zhu XR, Bader V, Linnartz B, Schmidt S, Lubbert H: Mono- and double-mutant mouse models of Parkinson's disease display severe mitochondrial damage. *Hum Mol Genet* 2007, 16:2377-2393.
 52. Cai X, Chiu YH, Chen ZJ: The cGAS-cGAMP-STING pathway of cytosolic DNA sensing and signaling. *Mol Cell* 2014, 54:289-296.
 53. Chen Q, Sun L, Chen ZJ: Regulation and function of the cGAS-STING pathway of cytosolic DNA sensing. *Nat Immunol* 2016, 17:1142-1149.
 54. Ablasser A, Goldeck M, Cavlar T, Deimling T, Witte G, Rohl I, Hopfner KP, Ludwig J, Hornung V: cGAS produces a 2'-5'-linked cyclic dinucleotide second messenger that activates STING. *Nature* 2013, 498:380-384.
 55. Barber GN: STING-dependent cytosolic DNA sensing pathways. *Trends Immunol* 2014, 35:88-93.
 56. Sliter DA, Martinez J, Hao L, Chen X, Sun N, Fischer TD, Burman JL, Li Y, Zhang Z, Narendra DP, Cai H, Borsche M, Klein C, Youle RJ: Parkin and PINK1 mitigate STING-induced inflammation. *Nature* 2018, 561:258-262.
 57. Brumovsky P, Villar MJ, Hokfelt T: Tyrosine hydroxylase is expressed in a subpopulation of small dorsal root ganglion neurons in the adult mouse. *Exp Neurol* 2006, 200:153-165.
 58. Lin CH, Chao CC, Wu SW, Hsieh PC, Feng FP, Lin YH, Chen YM, Wu RM, Hsieh ST: Pathophysiology of Small-Fiber Sensory System in Parkinson's Disease: Skin Innervation and Contact Heat Evoked Potential. *Medicine (Baltimore)* 2016, 95:e3058.
 59. Numazaki M, Tominaga M: Nociception and TRP Channels. *Curr Drug Targets CNS Neurol Disord* 2004, 3:479-485.
 60. Tominaga M, Caterina MJ: Thermosensation and pain. *J Neurobiol* 2004, 61:3-12.
 61. Brenneis C, Kistner K, Puopolo M, Segal D, Roberson D, Sisignano M, Labocha S, Ferreiros N, Strominger A, Cobos EJ, et al: Phenotyping the function of TRPV1-expressing sensory neurons by targeted axonal silencing. *J Neurosci* 2013, 33:315-326.
 62. Devigili G, Tugnoli V, Penza P, Camozzi F, Lombardi R, Melli G, Broglio L, Granieri E, Lauria G: The diagnostic criteria for small fibre neuropathy: from symptoms to neuropathology. *Brain* 2008, 131:1912-1925.
 63. Hayashida K, Oyanagi S, Mizutani Y, Yokochi M: An early cytoplasmic change before Lewy body maturation: an ultrastructural study of the substantia nigra from an autopsy case of juvenile parkinsonism. *Acta Neuropathol* 1993, 85:445-448.
 64. Trimmer PA, Swerdlow RH, Parks JK, Keeney P, Bennett JP, Jr., Miller SW, Davis RE, Parker WD, Jr.: Abnormal mitochondrial morphology in sporadic Parkinson's and Alzheimer's disease cybrid cell

- lines. *Exp Neurol* 2000, 162:37-50.
65. Roy S, Wolman L: Ultrastructural observations in Parkinsonism. *J Pathol* 1969, 99:39-44.
66. Garcia-Sanz P, Orgaz L, Fuentes JM, Vicario C, Moratalla R: Cholesterol and multilamellar bodies: Lysosomal dysfunction in GBA-Parkinson disease. *Autophagy* 2018, 11:1-2.
67. Magalhaes J, Gegg ME, Migdalska-Richards A, Doherty MK, Whitfield PD, Schapira AH: Autophagic lysosome reformation dysfunction in glucocerebrosidase deficient cells: relevance to Parkinson disease. *Hum Mol Genet* 2016, 25:3432-3445.
68. Ikenaka K, Suzuki M, Mochizuki H, Nagai Y: Lipids as Trans-Acting Effectors for alpha-Synuclein in the Pathogenesis of Parkinson's Disease. *Front Neurosci* 2019, 13:693.
69. Kilpatrick BS, Magalhaes J, Beavan MS, McNeill A, Gegg ME, Cleeter MW, Bloor-Young D, Churchill GC, Duchen MR, Schapira AH, Patel S: Endoplasmic reticulum and lysosomal Ca(2)(+) stores are remodelled in GBA1-linked Parkinson disease patient fibroblasts. *Cell Calcium* 2016, 59:12-20.
70. Bhave G, Hu HJ, Glauner KS, Zhu W, Wang H, Brasier DJ, Oxford GS, Gereau RWt: Protein kinase C phosphorylation sensitizes but does not activate the capsaicin receptor transient receptor potential vanilloid 1 (TRPV1). *Proc Natl Acad Sci U S A* 2003, 100:12480-12485.
71. Prescott ED, Julius D: A modular PIP2 binding site as a determinant of capsaicin receptor sensitivity. *Science* 2003, 300:1284-1288.
72. Van Buren JJ, Bhat S, Rotello R, Pauza ME, Premkumar LS: Sensitization and translocation of TRPV1 by insulin and IGF-I. *Mol Pain* 2005, 1:17.
73. Susankova K, Tousova K, Vyklicky L, Teisinger J, Vlachova V: Reducing and oxidizing agents sensitize heat-activated vanilloid receptor (TRPV1) current. *Mol Pharmacol* 2006, 70:383-394.
74. Rosenbaum T, Gordon-Shaag A, Munari M, Gordon SE: Ca²⁺/calmodulin modulates TRPV1 activation by capsaicin. *J Gen Physiol* 2004, 123:53-62.
75. Zhang X, Huang J, McNaughton PA: NGF rapidly increases membrane expression of TRPV1 heat-gated ion channels. *EMBO J* 2005, 24:4211-4223.
76. West AP, Khoury-Hanold W, Staron M, Tal MC, Pineda CM, Lang SM, Bestwick M, Duguay BA, Raimundo N, MacDuff DA, et al: Mitochondrial DNA stress primes the antiviral innate immune response. *Nature* 2015, 520:553-557.
77. Mathur V, Burai R, Vest RT, Bonanno LN, Lehallier B, Zardeneta ME, Mistry KN, Do D, Marsh SE, Abud EM, Blurton-Jones M, Li L, Lashuel HA, Wyss-Coray T: Activation of the STING-Dependent Type I Interferon Response Reduces Microglial Reactivity and Neuroinflammation. *Neuron* 2017, 96:1290-1302.e1296. doi: 1210.1016/j.neuron.2017.1211.1032.
78. Moy SS, Nadler JJ, Perez A, Barbaro RP, Johns JM, Magnuson TR, Piven J, Crawley JN: Sociability and preference for social novelty in five inbred strains: an approach to assess autistic-like behavior in mice. *Genes Brain Behav* 2004, 3:287-302.
79. Brunkhorst-Kanaan N, Klatt-Schreiner K, Hackel J, Schroter K, Trautmann S, Hahnefeld L, Wicker S, Reif A, Thomas D, Geisslinger G, Kittel-Schneider S, Tegeder I: Targeted lipidomics reveal

- derangement of ceramides in major depression and bipolar disorder. *Metabolism* 2019.
80. Waterston RH, Lindblad-Toh K, Birney E, Rogers J, Abril JF, Agarwal P, Agarwala R, Ainscough R, Alexandersson M, An P, et al: Initial sequencing and comparative analysis of the mouse genome. *Nature* 2002, 420:520-562.
81. Dennis G, Jr., Sherman BT, Hosack DA, Yang J, Gao W, Lane HC, Lempicki RA: DAVID: Database for Annotation, Visualization, and Integrated Discovery. *Genome Biol* 2003, 4:P3.
82. Subramanian A, Tamayo P, Mootha VK, Mukherjee S, Ebert BL, Gillette MA, Paulovich A, Pomeroy SL, Golub TR, Lander ES, Mesirov JP: Gene set enrichment analysis: a knowledge-based approach for interpreting genome-wide expression profiles. *Proc Natl Acad Sci U S A* 2005, 102:15545-15550.

Figures

Figure 1

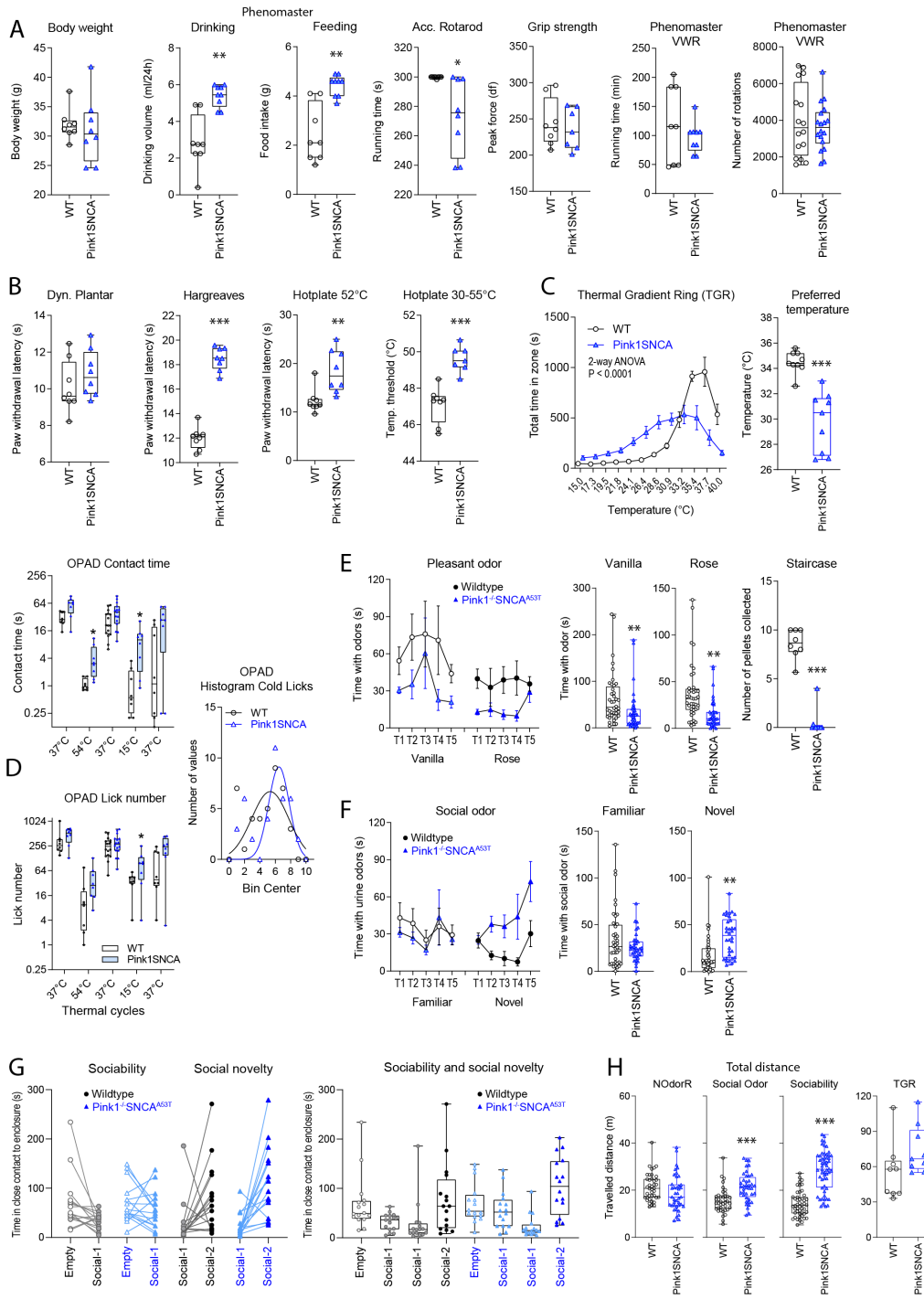


Figure 1

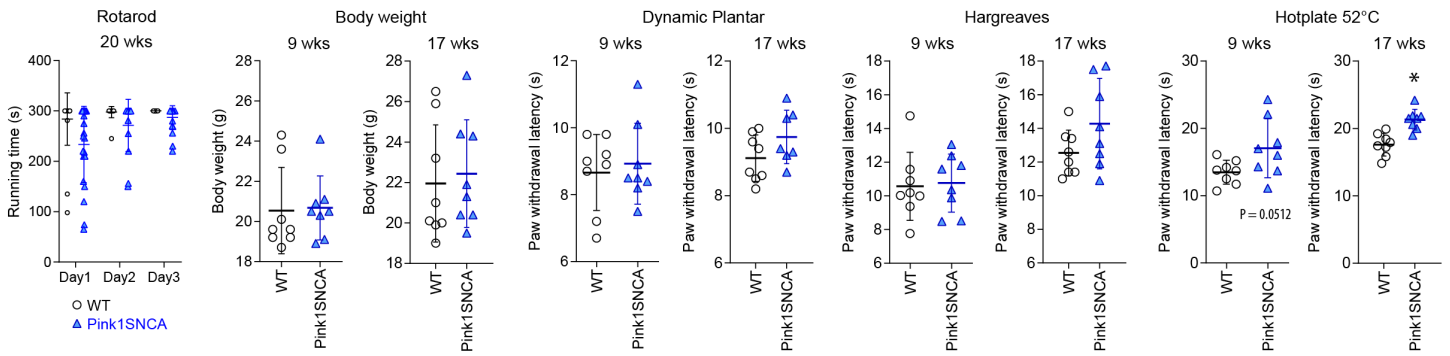
Behavior of middle-aged Pink1SNCA mice in motor and sensory function tests A: The box/scatter plots show exemplary body weights at 1 year of age. Drinking, feeding and voluntary wheel running (VWR) were recorded in Phenomaster cages (13 months old). Motor coordination and endurance was tested on an accelerating Rota Rod (9 months), and muscle strength with a grip strength meter (15 months). B: Nociceptive paw withdrawal latencies on mechanical (dynamic plantar test) and heat stimulation

(Hargreaves and Hot Plate) at 9 months of age. C: Preference temperatures on a Thermal Gradient Ring (TGR) with a temperature gradient of 15-40°C at 10 months of age. D: Trigeminal sensory functions assessed in an Orofacial Pain Assessment Device (OPAD). Box/Scatter plots show contact times with metal bars and lickings at the respective temperatures at 12 months of age. For the histogram, all licks at cold temperatures (7°C, 10°C and 15°C) were pooled, and fitted to a Gauss distribution. E: Olfactory sensation and preference of pleasant odors in a Novel Odor Recognition test (NOdorR) with vanilla and rose, at 16 months of age. The left panel shows the time spent with the odorous stimuli in successive trials. For the box plot summary, all tests with the respective odor were pooled. Hence each mouse is represented 5-times. The staircase test (right, 15 months) shows that Pink1SNCA mice did not reach out for the sweet pellets. F: In analogy to E, the plots show the behavior in a Novel Social Odor test, which used mixtures of urine as familiar and novel stimuli (14 months). G: Sociability and Social Novelty assessed the preference of a social compartment versus an empty compartment and subsequently the preference of a novel mouse over the familiar one (12 months old). For analysis, two successive trials were pooled. Hence, each mouse is represented twice. Results were compared with paired t-tests (left) and ANOVA (right). There were no difference between groups. H: Total distances travelled in different Maze tests and Thermal Gradient Ring (TGR) to assess spontaneous locomotion. Data from all trials were pooled and each scatter is one trial. The scatter show results of individual mice, which were 9-10 months old at start of the sensory tests, 9-15 months for motor function tests and 15-16 months for social tests. Age and gender matched pairs were used in all experiments. Sample sizes were 8-9 mice for all experiments. The box shows the interquartile range, the whisker show minimum to maximum. Groups were compared with unpaired, two-sided Student's t-tests, except in G (paired ttest and ANOVA). Asterisks show significant difference at * $P < 0.05$, ** $P < 0.001$, *** $P < 0.0001$.

Figure 2

A

Young double mutant mice: motor and sensory functions



Single mutant mice: motor & sensory functions

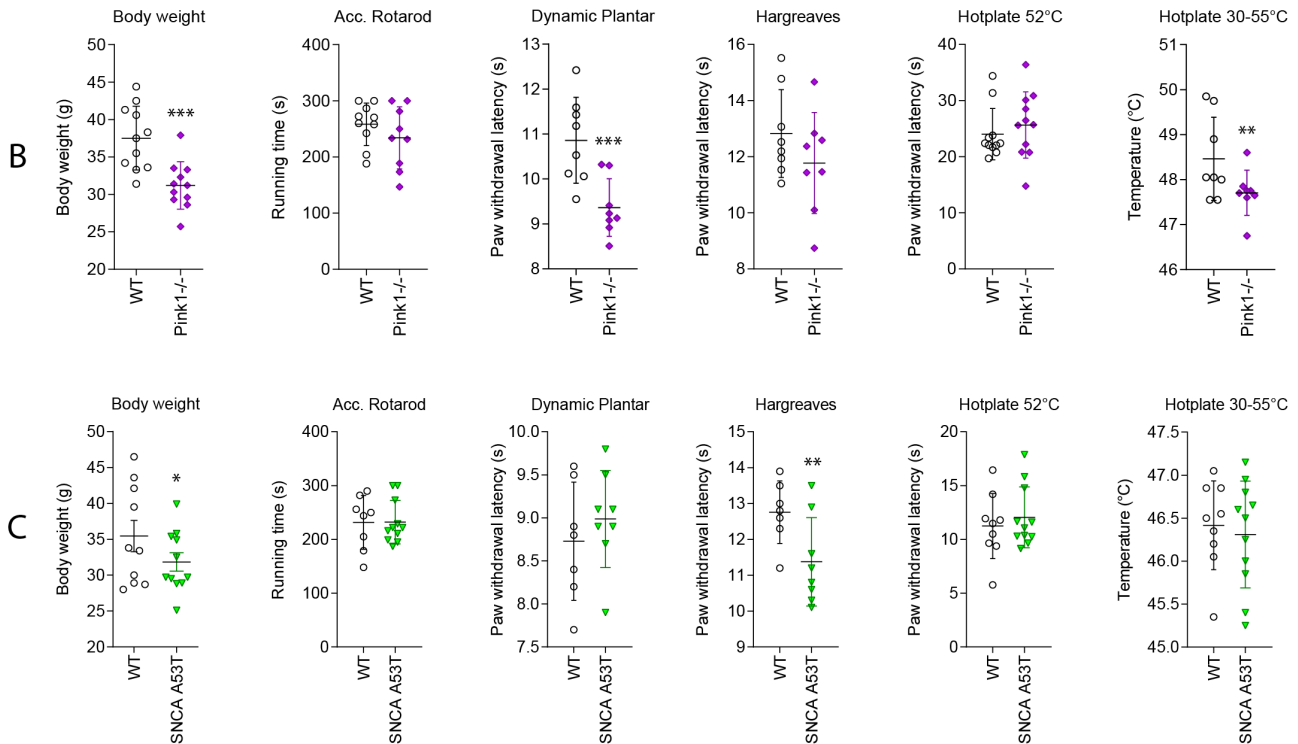


Figure 2

Behavior of young Pink1SNCA mice and of single mutant mice A: Rota Rod running performance and nociceptive paw withdrawal latencies on mechanical (dynamic plantar test) and heat stimulation (Hargreaves and Hot Plate) in young Pink1SNCA double mutant mice at 9 weeks and 17 weeks of age. The Rota Rod training consisted in three trials per training day, so that every mouse is represented with 3 runs per day. B: Rota Rod running and nociceptive paw withdrawal latencies on mechanical (dynamic plantar test) and heat stimulation (Hargreaves and Hot Plate) in 9-10 months old Pink1^{-/-} mice and the

respective wildtype control mice. C: Behavior as in B in 9-10 months old SNCA-A53T single mutant and control mice. The scatter show results of individual mice. Age and gender matched pairs were used in all experiments, n = 8 per group. The line is the mean, the whisker show standard deviations (SD). Groups were compared with unpaired, two-sided Student's t-tests, Asterisks show significant differences between groups, *P<0.05, **P<0.001, ***P<0.0001.

Figure 3

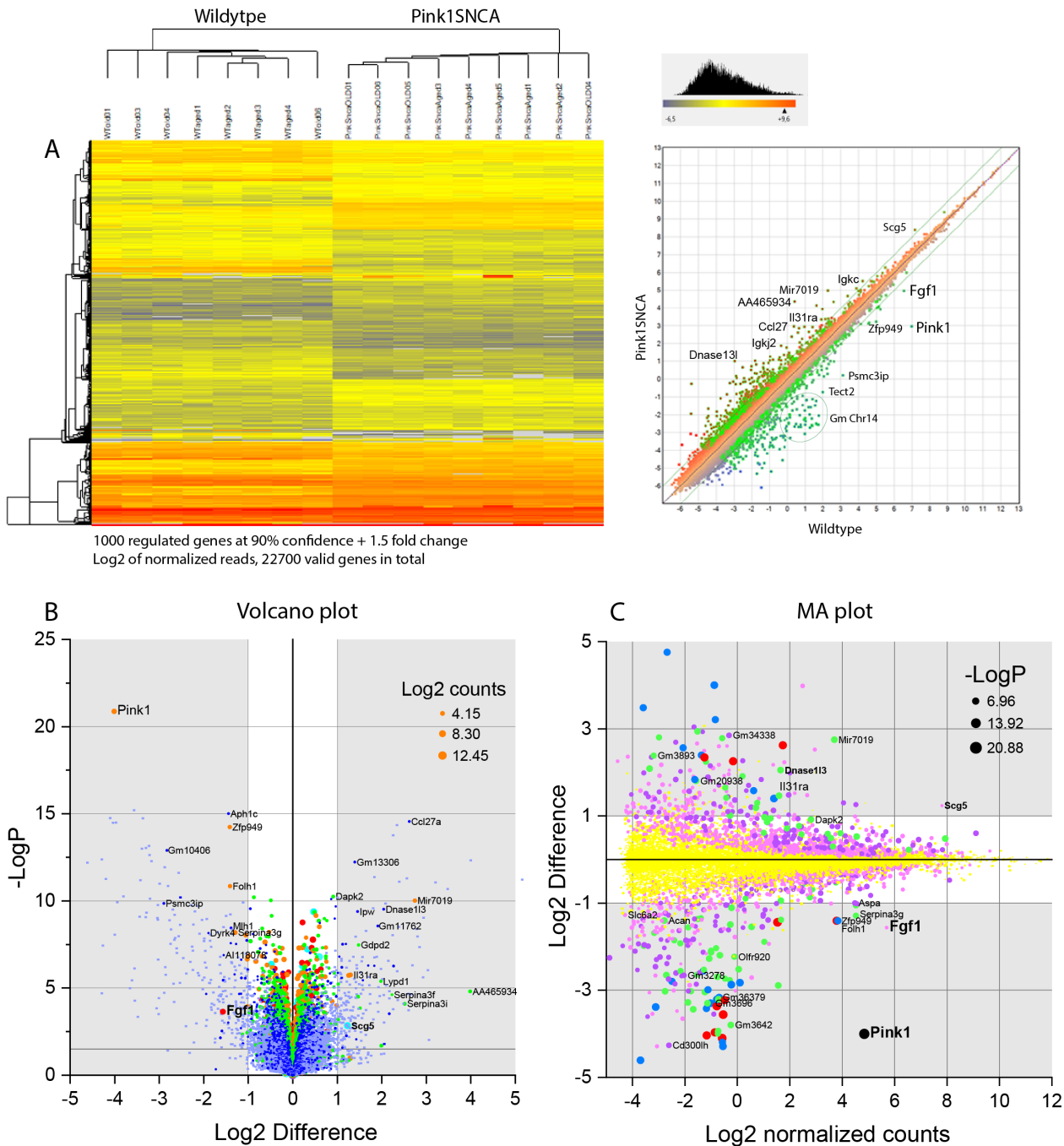


Figure 3

Gene expression analysis by RNA sequencing in dorsal root ganglia (DRGs) A: Scatter plot of the mean normalized counts (Log₂) of wildtype control mice (X-axis) and Pink1SNCA mice (Y-axis) and heat map of top 1000 regulated genes. Mice were middle aged (10-12 months, 4 and 5) and old (18 months, each 4) at the time of tissue preparation. All mice per group were analyzed together. The green dots in the scatter plot (right) show the genes, which were significant at 90% confidence level plus 1.5fold change and are represented in the heatmap. Mice and genes were clustered according to Euclidean distance metrics. The dendrogram of the mice (on top) shows a clear genotype separation based on differential gene expression. There was no age-dependent structure. B: Volcano bubble pots showing the Log₂ difference of the normalized counts on the X-axis versus the negative logarithm of the P-value of the t-test on the Y-axis. The size of the dots and the color indicates total abundance according to the log₂ normalized counts. Hence, the larger the dot, the stronger is the overall expression of the respective gene. Prominent hits are labeled with the gene symbol. B: MA bubble plots showing log₂ normalized counts on the X-axis versus the log₂ difference on the Y-axis. The dot size and color are coded according to the negative logarithm of the P-value of the t-test. Hence, the larger the dot, the stronger was the statistical difference between the genotypes. Prominent hits are labeled with the gene symbol. A log₂ difference of 1 shows a 2-fold change.

Figure 4

Calcium influx DRG neurons

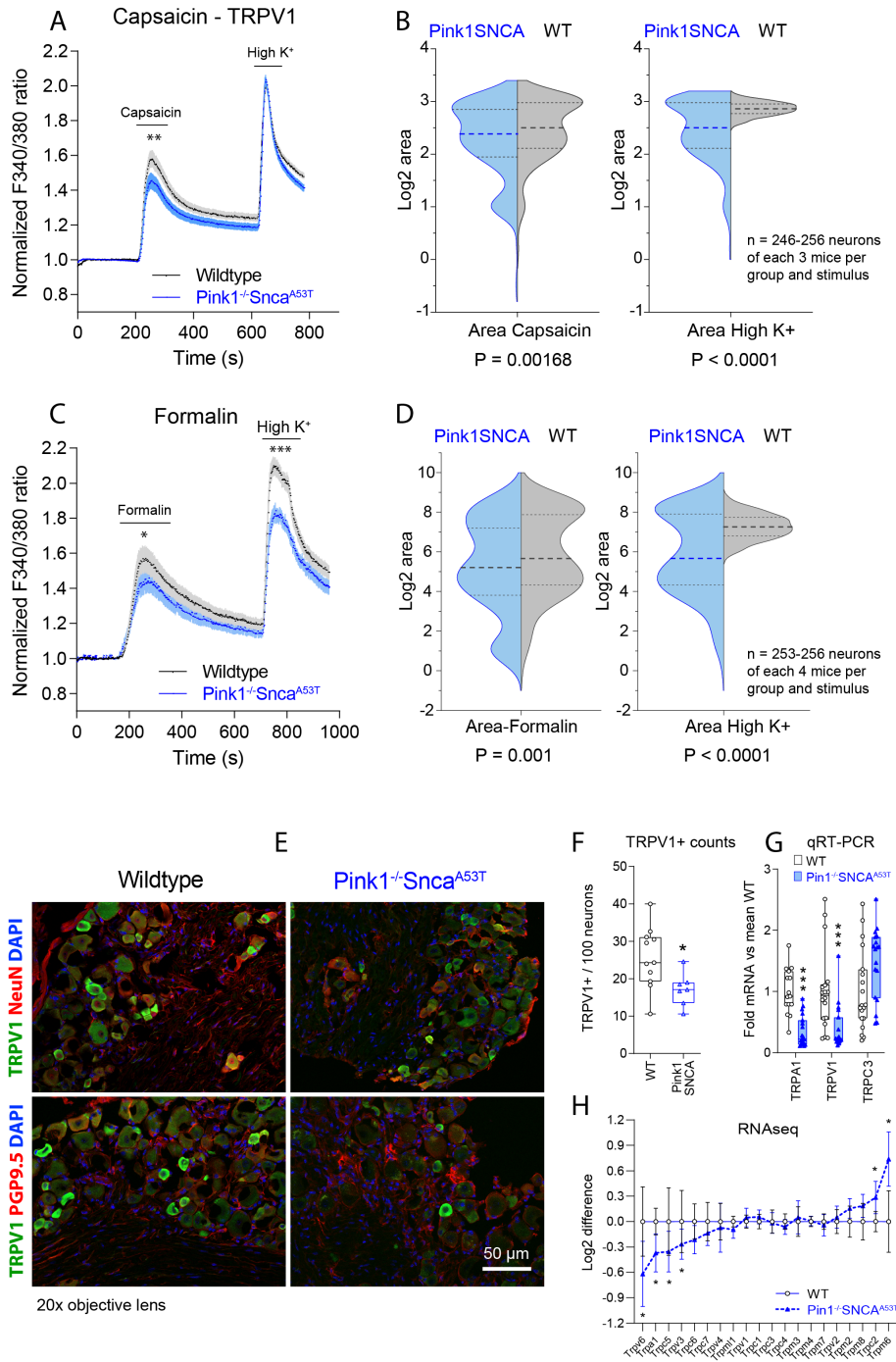


Figure 4

Calcium imaging and expression of TRP channels in DRGs A: Time course of calcium influx in primary DRG neurons of Pink1SNCA and wildtype control mice on stimulation with capsaicin (1 μM from 180-206 s) to stimulate TRPV1 channels and with high K+ (100 mM KCl, from 600-630 s) to evoke depolarization-evoked calcium currents. Data are means ± sem of 246 and 256 neurons (Pink1SNCA and WT) of 10-12 cultures of each 3 mice per group, which were 18 months old. All neurons responding to high K+ with >1.5

fold increase of $[Ca^{2+}]_i$ were included in the analysis. Calcium fluxes were determined as absorbance ratio of Fura2 at excitation wavelengths of 340 and 380 nm. Ratios were normalized to the mean baseline ratio, set to 1. B: Half violin plots of the log₂-transformed areas under the peak calcium versus time curves (AUCs) of the neurons shown in A. AUCs were determined by integration from 198-500 s for capsaicin and 600-778 s for high K⁺. The thick dashed line shows the median, the dotted lines show the interquartile range. The violin shows the distribution, obtained by Kernel density estimation. C: In analogy to A, time courses of calcium influx upon stimulation of DRG neurons with formalin (0.01% from 100-200 s) to stimulate TRPA1 channels and with high K⁺ (100 mM KCl from 680-780 s). Data are means \pm sem of 253 and 256 neurons (Pink1SNCA and WT) of 12-14 cultures of each 4 mice per group, which were 18 months old. D: In analogy to B, half violin plots show Log₂ transformed AUCs of neurons presented in C. AUCs were determined by integration from 175-520 s for formalin and 695-950 s for high K⁺. Peaks and AUCs were compared with 2-sided, unpaired t-tests, time courses by 2-way ANOVA. *P<0.05, **P<0.001, ***P<0.0001. E, F: Immunofluorescence analysis of TRPV1 expression in DRGs of Pink1SNCA and wildtype control mice at 18 months of age. Each two exemplary images in E, quantification in F. Each scatter represents a stitched DRG section of 3-4 mice per group. G: Quantitative rt-PCR analysis of TRP channel gene expression in DRGs of Pink1SNCA and wildtype control mice, which were 7 months (each group n = 7) and 16-18 months old (each group n = 4). Each scatter represents a mouse. Expression of each gene was analyzed separately per 2-tailed, unpaired Student's t-test. Different ages were pooled. H: RNA sequencing results of TRP channel expression in DRGs (mice as explained in Fig. 3). For comparison, the reads were normalized to the mean log₂ counts of wildtype control mice, and they are expressed as the log₂ difference. Data were compared per 2-way ANOVA and multiple comparisons corrected for the False Discovery Rate (FDR) according to Benjamini, Krieger and Yekutieli. Asterisks indicate multiplicity adjusted P values, *P<0.05.

Figure 5

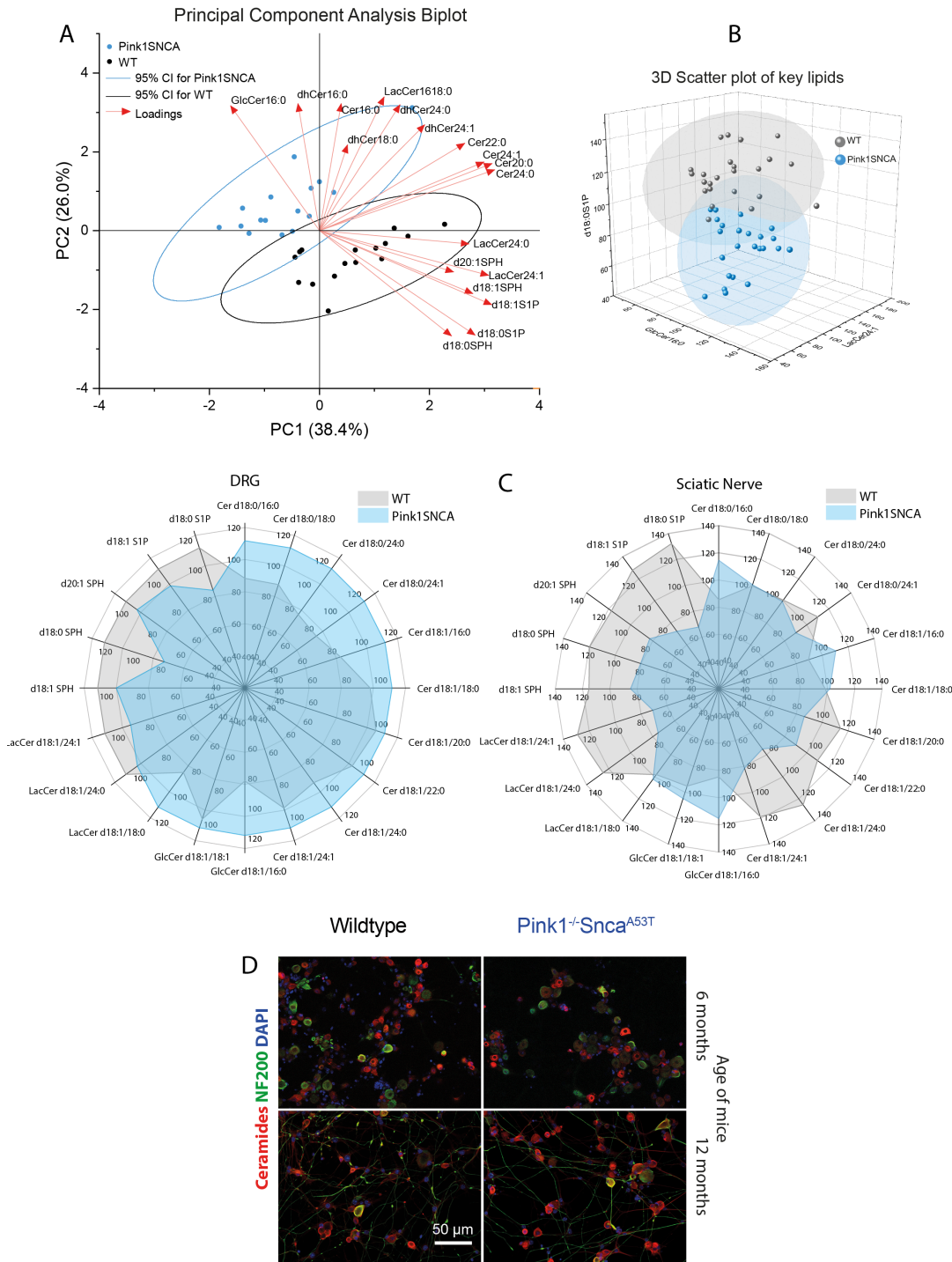


Figure 5

Sphingolipids in DRGs, sciatic nerve and spinal cord A: Principal component analysis (PCA) biplot of lipids levels in DRGs and sciatic nerve (ScN) of 8 mice per group (age 12 months), using a grouping according to genotype. Percentages were used as PCA input because total lipid concentrations differ by several orders of magnitude. The respective lipid mean of all samples was set to 100%. The loadings are presented as arrows. The dots are individual mice, and each mouse is represented twice for DRG and

ScN. The ellipses show the 95% CI. B: 3D scatter plot of three lipid species of three classes, which differed most between genotypes: GlcCer 16:0, sphinganine (d18:0 SPH) and LacCer 24:1. The data are percentages of each lipid (relative to the mean set to 100%) for each tissue. Hence, each mouse is represented 3-times for DRG, ScN and SC. The ellipsoids show the 95% CI. C: Polar plots of the mean lipid percentages in the DRGs and sciatic nerve (SC in Suppl. Fig. 5). D: Immunofluorescence analysis of ceramides in primary DRG cultures at different ages of the mice. DAPI was used as nuclear counterstain to assess the cellularity and neurofilament of 200 kDa (NF200) to stain neurons and dendrites.

Figure 6

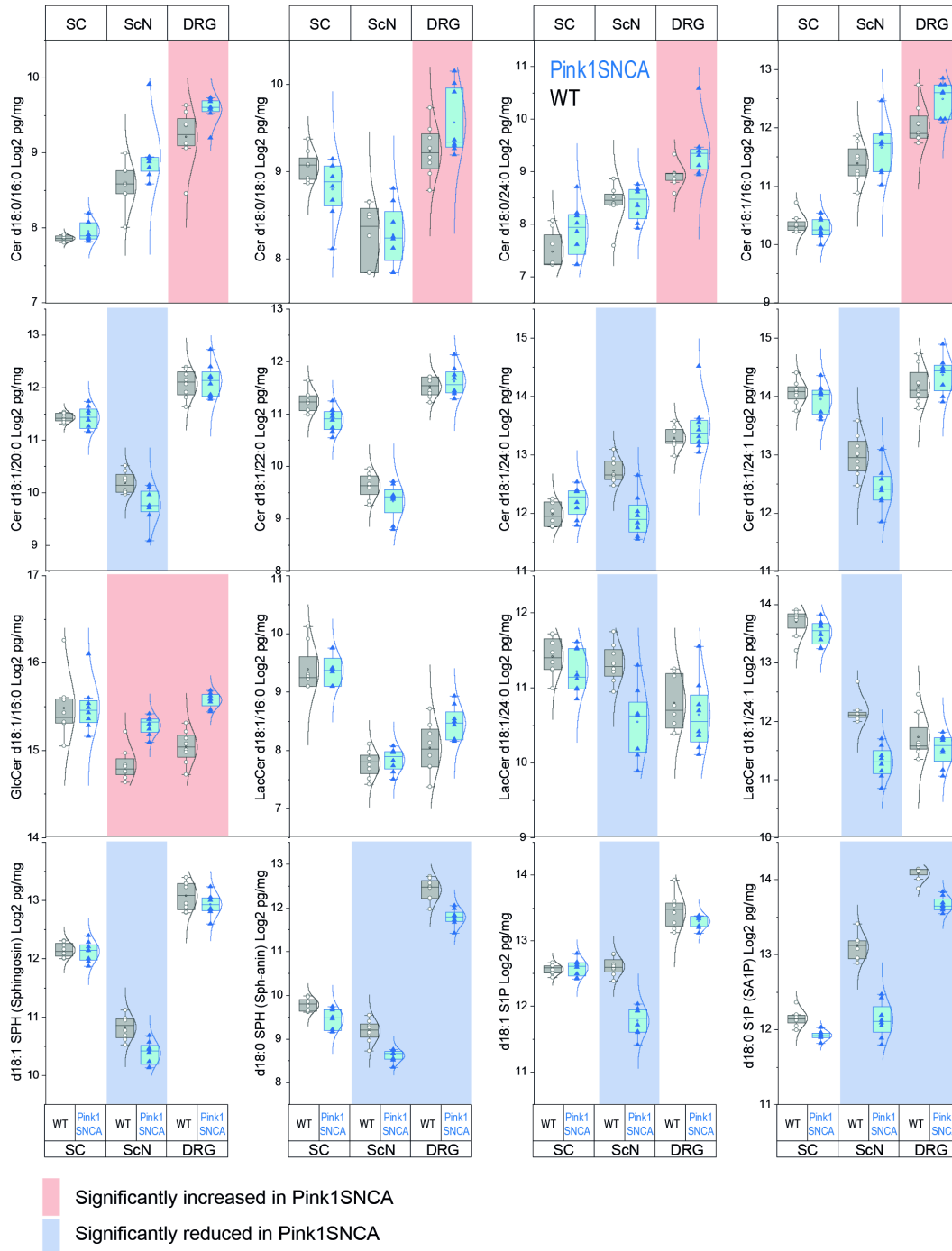


Figure 6

Tissue specific analysis of sphingolipid species in DRGs, sciatic nerve and spinal cord Box/scatter plots show the concentrations of the respective lipids (Y-axis labeling) in pg/mg of tissue in spinal cord (SC), sciatic nerve (ScN) and DRGs in 12 months old Pink1SNCA and wildtype control mice (n = 8 per group, all three tissues analyzed per mouse). Each scatter represents a mouse. The boxes show the interquartile range, the line is the median, the small open circle is the mean, the whiskers show minimum to maximum and the line shows the distribution according to a Gauss fit. Data were compared with 2-way ANOVA for each lipid separately, followed by posthoc t-tests using an adjustment of alpha according to Holm-Šidák. Lipids and sites where genotypes differed significantly are color-coded. Red indicates a significant increase and blue a significant decrease.

Figure 7 Exemplary mouse pair #4

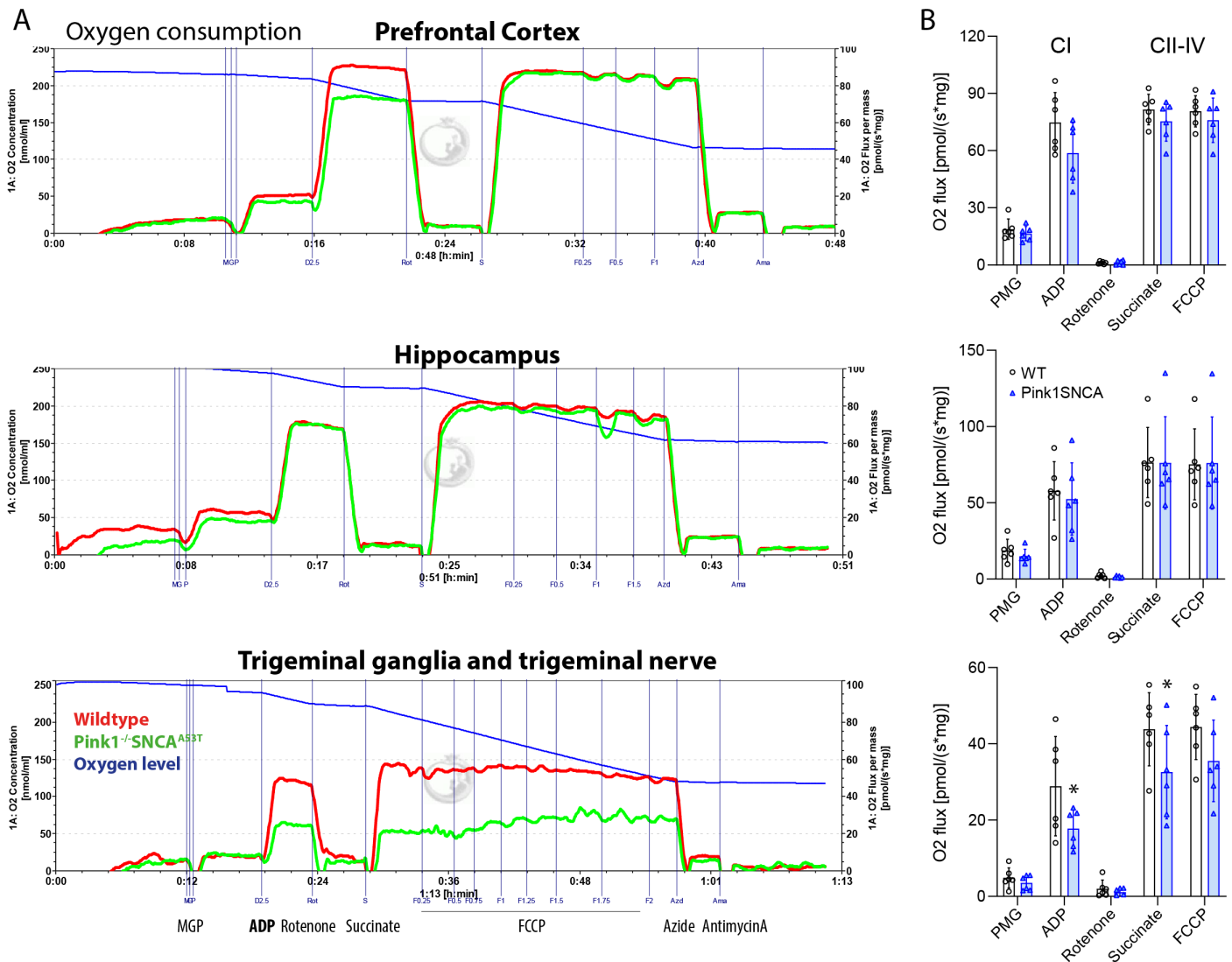


Figure 7

Oxygraph respirometry in cortex, hippocampus and trigeminal ganglia A: Exemplary respirograms of each one Pink1SNCA and wildtype control mice in freshly prepared homogenates of the prefrontal cortex, hippocampus, trigeminal ganglia and trigeminal nerve. B: Quantitative OXPHOS analysis of each 6 mice per genotype for each site. Mitochondrial respiration was quantified as oxygen flux. LEAK-respiration was induced by adding pyruvate, malate and glutamate (PMG, CI substrates). CI-respiration was initiated by adding ADP in a saturating concentration. To measure CII respiration, rotenone was added to block CI, followed by adding succinate. Maximum uncoupled respiration was measured after stepwise titration with the uncoupler, FCCP. Residual oxygen consumption (ROX) was determined after sequential inhibition of complex III with antimycin A and complex IV with azide. Absolute respiration rates were corrected for ROX and normalized for the protein content. Data were analyzed per 2-way ANOVA and subsequent genotype comparisons for each period using t-tests. Asterisks indicate significant differences between groups, *P < 0.05.

Figure 8

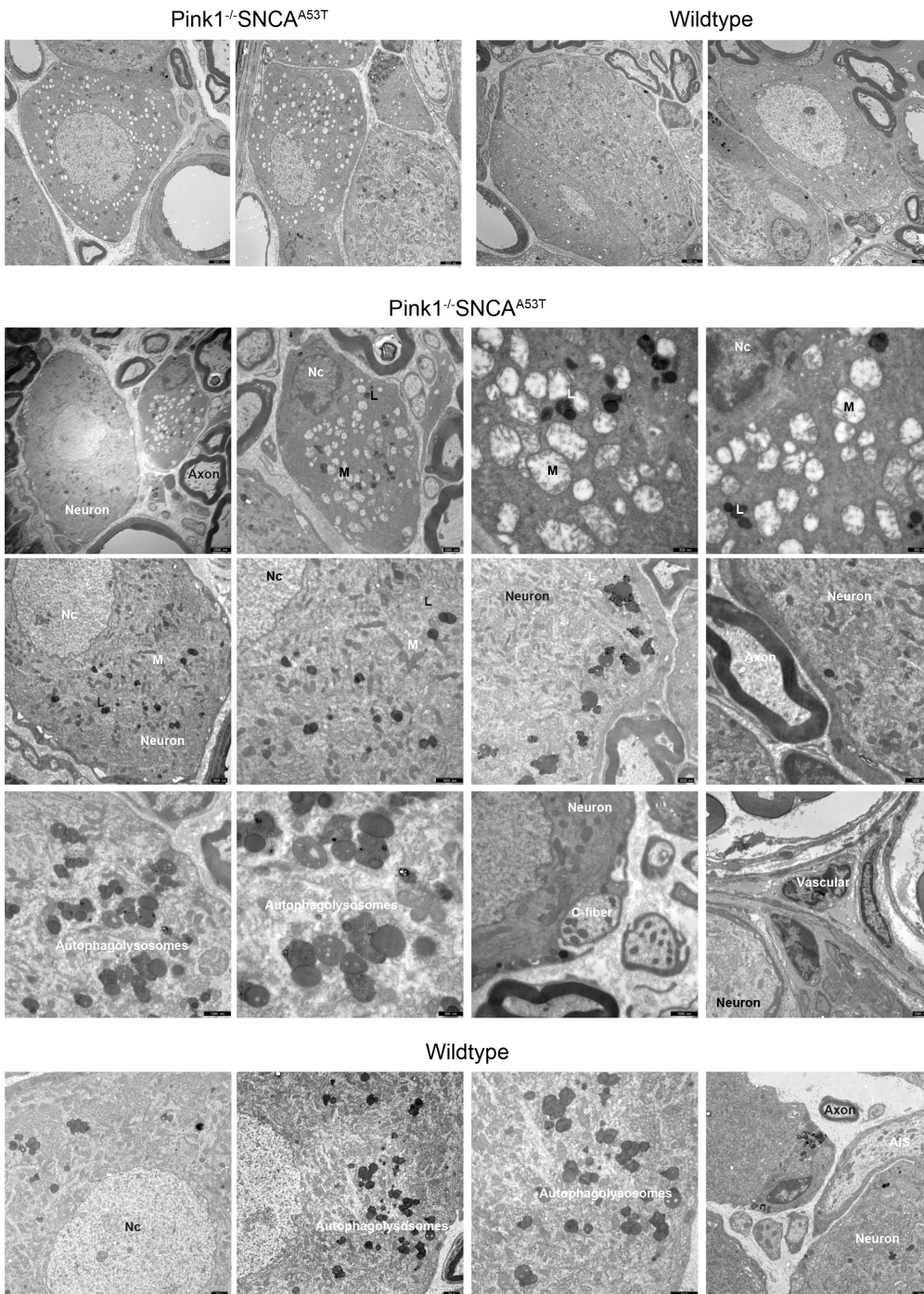


Figure 8

Transmission electron microscopy of DRGs and ultrastructural analysis of mitochondria TEM studies were performed in Pink1SNCA and wildtype control mice at 15-17 months of age, n = 3 per genotype, ages matched. The upper panel gives each two examples of cells with white mitochondria, which were more prominent in Pink1SNCA mice and these mitochondria appeared to be swollen. The lower panel shows different cell types and organelles in exemplary images of Pink1SNCA and comparable images of

wildtype mice. Neurons with dark 'cisterna type' mitochondria did not differ between genotypes. Myelin sheaths, axons, vascular cells are satellite cells did not show overt differences. Prominent lysosomes were present in neurons of both genotypes. AIS = axon initial segment, M = mitochondria, L = lysosome.

Figure 9

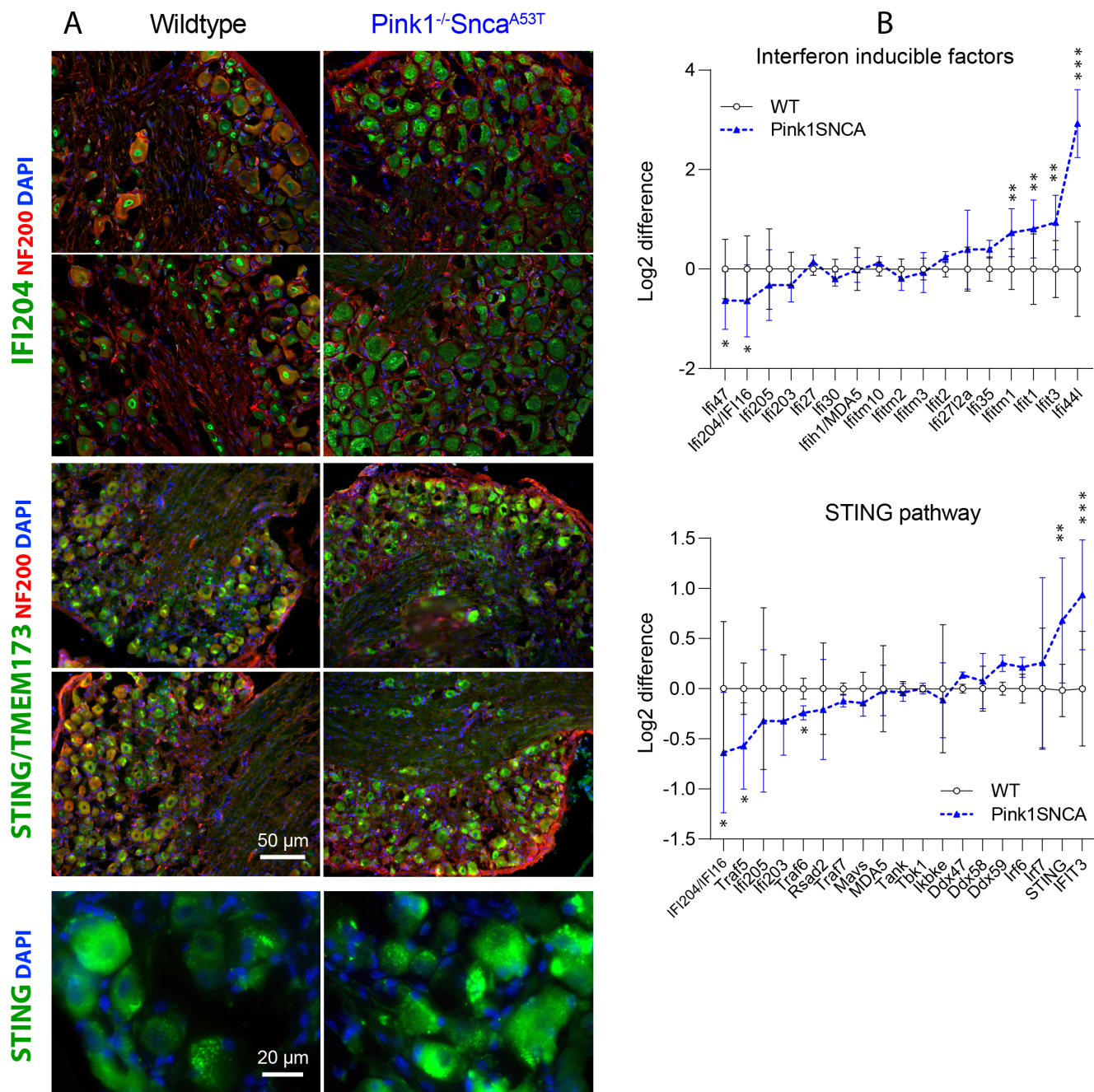


Figure 9

Immunofluorescence and RNAseq analysis of innate immune pathways A: Exemplary immunofluorescence images (each 2 images of 3-4 mice per group, 18 months old) of the cytosolic DNA

sensor, gamma-interferon-inducible protein, IFI204 (murine homolog of human IFI16), which activate cGAS-cGAMP-STING/TMEM173 signaling. STING images are shown in the bottom panel. IFI204/IFI16 localizes to the nucleus on stimulation and redistributes to the cytosol depending on the acetylation of the nuclear localization signal. In Pink1SNCA, IFI204 was less confined to the nucleus. STING is activated by binding cGMAP, translocates from the ER, is then phosphorylated by TBK1 and activates interferon regulatory factors (IRF) and subsequently, type I interferon responses. STING mostly localized to the perinuclear ER of DRG neurons in both genotypes. B: Gene expression analysis by RNA sequencing in the DRGs of middle-aged and old Pink1SNCA (n = 9) and wildtype control mice (n = 8; mice as explained in Fig. 3) of interferon inducible factors and of STING pathway associated genes. For comparison, the reads were normalized to the mean log2 counts of wildtype control mice, and they are expressed as the log2 difference. Data were compared per 2-way ANOVA and multiple comparisons corrected for the False Discovery Rate (FDR) according to Benjamini, Krieger and Yekutieli. Asterisks indicate multiplicity adjusted P values, *P<0.05, **P<0.01, ***P<0.0001.

Supplementary Files

This is a list of supplementary files associated with this preprint. Click to download.

- [SuplTablesSuplFigsLegendsPink1SNCA sensory20200315.docx](#)